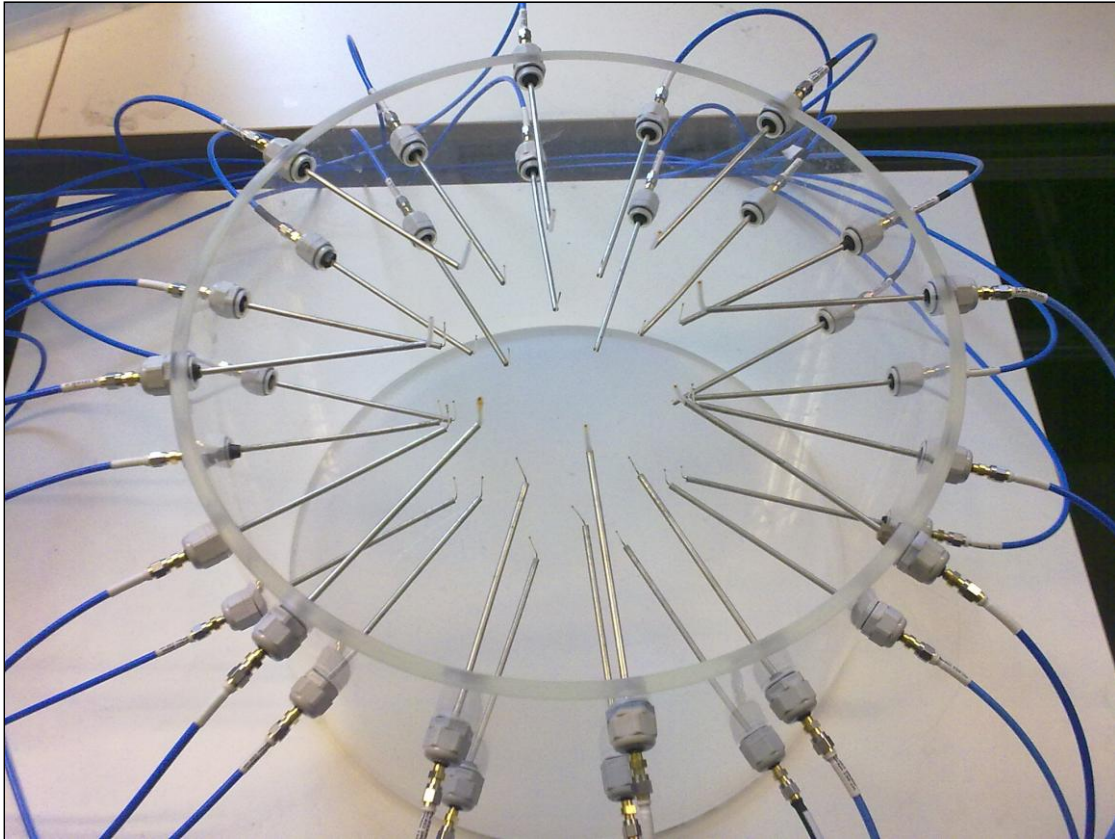


# CHALMERS



## Image reconstructions and FDTD modelling of an antenna array for 3D microwave tomography

*Master of Science Thesis*

**JOHAN KÖSTER**

Department of Signals and Systems  
Division of Biomedical Engineering  
CHALMERS UNIVERSITY OF TECHNOLOGY  
Göteborg, Sweden, 2011  
Report No. EX022/2011

Image reconstructions and FDTD modelling of an antenna array for 3D  
microwave tomography  
JOHAN KÖSTER

© JOHAN KÖSTER, 2011.

Technical report no EX022/2011  
Department of Signals and Systems  
Division of Biomedical Engineering  
Chalmers University of Technology  
SE-412 96 Göteborg Sweden  
Telephone +46-(0)31 772 10 00

Cover: The cover shows the resulting antenna array.

Chalmers Tekniska Högskola  
Göteborg, Sweden 2011

---

## Abstract

Image reconstructions and FDTD modelling of an antenna array for 3D microwave tomography

JOHAN KÖSTER

Department of Signals and Systems

Division of Biomedical Engineering

Chalmers University of Technology

Breast cancer is the most common type of cancer for women worldwide and thus considered to be a great problem. Early detection improves the chances of successful treatment, however a self diagnosis of this type of cancer is quite hard and this is why an accurate diagnosis method is very interesting. The use of microwave tomography is not widespread in the medical field due to lack of clinical success and an extension from two dimensions to three could be a solution to this problem. One of the reasons for using microwave tomography as a mammography tool is that the contrast between a tumour and healthy tissue is large and the radiation used is not ionising. Another reason is that the cost is relatively low in comparison to other soft tissue imaging tools such as magnetic resonance imaging.

Five different types of monopole antennas were modelled using FDTD and evaluated as well as the placement of the antennas and cables in respect to each other. Simulations of the resulting antenna array were performed and matched the measurements well. The reconstructions performed with measured data from the developed antenna array imaged objects well in the vertical direction as well as in the horizontal direction. The permittivity of a small high contrast object was successfully reconstructed as well as of a larger low contrast object. The reconstruction of the permittivity for two small high contrast objects was successful and the two objects are detected. Consistently the conductivity was not well reconstructed for any object.

**Keywords:** 3D microwave tomography, antenna modelling, FDTD, image reconstruction, mammography



# Acknowledgements

I would like to thank my supervisor Assistant Professor Andreas Fhager for his guidance throughout the work. I also would like to thank Assistant Professor Tonny Rubæk for his input.

The computations were performed on C3SE computing resources.



# Contents

<b>Contents</b>	<b>vii</b>
<b>1 Introduction</b>	<b>1</b>
1.1 Background . . . . .	1
1.1.1 Purpose . . . . .	1
1.2 Microwave tomography . . . . .	2
1.2.1 Image reconstructions . . . . .	3
<b>2 The FDTD method</b>	<b>5</b>
2.1 Maxwell's equations . . . . .	5
2.2 The Yee lattice . . . . .	6
2.2.1 Discretisation . . . . .	8
2.3 Electromagnetic source . . . . .	8
2.3.1 Hard source . . . . .	8
2.3.2 Resistive voltage source . . . . .	9
2.3.3 Thin wire . . . . .	10
2.4 Absorbing boundary conditions . . . . .	10
<b>3 Reconstruction of dielectric properties</b>	<b>13</b>
3.1 Dielectric properties of human tissues . . . . .	13
3.1.1 Dispersive response . . . . .	13
3.1.2 Relaxation process . . . . .	14
3.2 Measure procedure . . . . .	15
3.3 The reconstruction algorithm . . . . .	16
<b>4 Modelling of the antenna array</b>	<b>19</b>
4.1 Antennas in an infinite large water tank . . . . .	19
4.1.1 Length and frequency . . . . .	19
4.1.2 Evaluation of different antennas in water . . . . .	20
4.2 Modelling of the measuring tank . . . . .	29
4.2.1 Edge effects . . . . .	29

## CONTENTS

---

4.3	Modelling of the whole antenna array . . . . .	31
4.3.1	FDTD grid coordinate axes . . . . .	32
4.3.2	Measurement compared to simulation . . . . .	36
4.4	Summary of antenna modelling . . . . .	39
<b>5</b>	<b>Reconstructed images</b>	<b>41</b>
5.1	Homogeneous objects in water . . . . .	41
5.1.1	One small object . . . . .	42
5.1.2	Two small objects . . . . .	44
5.1.3	One large object . . . . .	46
5.1.4	Evaluation of measurements . . . . .	50
<b>6</b>	<b>Conclusion</b>	<b>53</b>
	<b>References</b>	<b>55</b>

# Chapter 1

## Introduction

### 1.1 Background

Breast cancer is the most common type of cancer for women worldwide and the risk of fatality can be lowered if the cancer is detected early [1]. The traditional method of breast cancer screening is to use low doses of X-ray, however there are alternatives. Microwave tomography research has increased in popularity as a medical diagnostics imaging tool as the radiation emitted is not ionising and the overall system is relatively cost effective. Furthermore the contrast between the tumour and the healthy tissue is high. The clinical use of microwave tomography is however not widespread due to lack of clinical success. One way of improving the clinical success could be to extend the ordinary two-dimensional microwave tomography to three-dimensions [2].

There have been some attempts to reconstruct three-dimensional objects with antennas positioned in a single circular plane [3], however the part of the object that is outside of the plane will not be reconstructed. Instead an assumption that the properties of the object are constant outside must be made. Therefore a new antenna array which allows measuring in different heights will be useful. In Meaney et al. 2009 [4] a two dimensional plane with antennas is moving up and down allowing for measurements on different heights but there is still no measuring of scattering in the z-direction only x- and y-direction.

#### 1.1.1 Purpose

The purpose of this thesis is to simulate and construct an antenna array for three-dimensional microwave tomography. There exist a two dimensional antenna array at the department but this has limitations and to

overcome these, the new array must be able to measure real world objects with width, depth and height. The main purpose of the new antenna array is to be used in a clinical test and evaluate if the three-dimensional microwave tomography can be used as a mammography tools to detect tumours. This is however not covered in this thesis.

## 1.2 Microwave tomography

Microwave tomography is different to computer tomography which uses non-diffracting sources such as X-rays. The main difference is that microwave tomography uses diffracting sources i.e. electromagnetic radiation which is not ionising and is thus safer to use. However the image obtained is not an illustration in matter of density but rather the imaged objects' dielectric properties i.e. conductivity,  $\sigma$ , and permittivity,  $\epsilon$ . This can be very useful as Fricke and Morse 1926 [5] discovered that the permittivity changes at 20 kHz for a cancer tumour.

### Tomography

Tomography is an imaging technique in which the object that is to be imaged is not just a projection of the real three dimensional object onto a two dimensional plane like an ordinary camera. Instead there are several different slices which can be viewed independently. This is very useful in medical diagnostics as more information can be given than just an ordinary image of the patient e.g. an examination can occur on a dept that is interesting from different injuries and diseases [6].

### Microwaves

Microwaves are defined as electromagnetic radiation with a frequency range of 300 MHz up to 300 GHz which is equivalent to a wavelength range of one meter to one millimetre. In these ranges the radiation is non-ionising which is preferable when examining human tissue.

### Mammography

Mammography is traditionally defined as the imaging technique which uses low energy X-rays to obtain an image of the human breast showing possible tumours. However microwave tomography can be used to investigate the dielectric properties of the human breast at different frequencies which can

give an idea of the breast contains breast tissue, fat or a malignant or benign tumour.

### 1.2.1 Image reconstructions

The image of the dielectric properties is reconstructed from measurement data obtained from an antenna array placed in a tank with the object that shall be imaged. The antenna array consists of several different rings of antennas placed inside an acrylic tank containing a liquid medium e.g. water. The antennas have similar construction as a coaxial cable with a metal wire encapsulated with a dielectric and a conductive layer. The transmitting part of the antenna will be the wire exposed in the outermost part of the antenna. One antenna sends a signal from a network analyser and all the other antennas are receiving one at the time and this is repeated for all antennas so that they have all received and all sent a signal. The network analyser has two ports so a multiplexer is connected in between. The multiplexer is controlled by a computer which saves all reflection,  $S_{11}$ , and all transmission,  $S_{21}$ , coefficients which later are used in the reconstruction which gives an image of the examined object. The reconstruction procedure is necessary as an image cannot be obtained by direct inversion of the measured data, instead a cost functional is defined and minimised. This functional is defined as the difference between the measured electric field at the antennas and several simulated electric fields with varying dielectric properties between the antennas. In Chapter 3 the reconstruction of the dielectric properties is described.

The simulated antennas are modelled with the Finite-Difference Time-Domain method which is a common numerical method for solving electromagnetic problems and this method is described in detail in Chapter 2. The antennas must have a cable connecting them to the multiplexer and as the antennas radiate in a radial symmetry they must be bent which is modelled in five different ways. The bending gives the antennas different properties and this effect as well as the placement of the antennas in the tank is covered in Chapter 4. The resulting images and the evaluation of the reconstruction can be seen in Chapter 5.



# Chapter 2

## The FDTD method

The Finite-Difference Time-Domain method is widely used to solve electromagnetic problems, one of the main reasons is the simplicity of the algorithm. The fact that the algorithm is solved in the time domain which gives a wide range of frequencies in just one simulation is another.

### 2.1 Maxwell's equations

Maxwell's equations are used when solving electromagnetic problems for non-complex geometries, otherwise a numerical method is necessary as the analytical solution will be impossible. Maxwell's equations on differential form are stated as follows:

$$\nabla \cdot \mathbf{D} = \rho_{free} \quad (2.1.1)$$

$$\nabla \cdot \mathbf{B} = 0 \quad (2.1.2)$$

$$\nabla \times \mathbf{E} = -\frac{\partial \mathbf{B}}{\partial t} \quad (2.1.3)$$

$$\nabla \times \mathbf{H} = \mathbf{J}_e + \frac{\partial \mathbf{D}}{\partial t} \quad (2.1.4)$$

In the reality there is often a dielectric material or a magnetic material which alters how the electromagnetic wave changes during propagation. The equations below describe how the material properties are related to the specific material property.

$$\mathbf{D} = \epsilon \mathbf{E} \quad (2.1.5)$$

$$\mathbf{B} = \mu \mathbf{H} \quad (2.1.6)$$

$$\mathbf{J}_e = \sigma \mathbf{E} \quad (2.1.7)$$

The permittivity,  $\epsilon$ , can be described as the resistance a propagating electric field meets in an insulator. This is due to the materials ability to be polarised when exposed to an electric field thus minimising the electric field inside the material. The permeability,  $\mu$ , is the equivalent of permittivity for a magnetic field instead of an electric field. The permeability is thus the materials ability to be magnetised due to a magnetic field. The conductivity,  $\sigma$ , is the materials ability to conduct a current.

## 2.2 The Yee lattice

Yee dived Maxwell's equations in their Cartesian coordinate system components [7]. The  $\mathbf{H}$ - and  $\mathbf{E}$ -fields are then solved in one grid at the time. A grid consists of either the  $\mathbf{H}$ - or  $\mathbf{E}$ -field component centred in the middle and are surrounded by four of the opposite components. The field components can be illustrated in a figure which is called the Yee cell. Figure 2.2.1 illustrates how the different field components are related to each other. There is now easy to see that the  $\mathbf{E}$ - and  $\mathbf{H}$ -components are separated in space, however in Yee's method they are also separated in time. First a time step must be chosen and thereafter the  $\mathbf{E}$ -field is computed in space and time with the  $\mathbf{H}$ -field data from neighbouring spatial points although the time point for the  $\mathbf{H}$ -field is the previous according to the  $\mathbf{E}$ -field.

$$\frac{\partial H_x}{\partial t} = \frac{1}{\mu} \left( \frac{\partial E_y}{\partial z} - \frac{\partial E_z}{\partial y} \right) \quad (2.2.1)$$

$$\frac{\partial H_y}{\partial t} = \frac{1}{\mu} \left( \frac{\partial E_z}{\partial x} - \frac{\partial E_x}{\partial z} \right) \quad (2.2.2)$$

$$\frac{\partial H_z}{\partial t} = \frac{1}{\mu} \left( \frac{\partial E_x}{\partial y} - \frac{\partial E_y}{\partial x} \right) \quad (2.2.3)$$

$$\frac{\partial E_x}{\partial t} = \frac{1}{\epsilon} \left( \frac{\partial H_z}{\partial y} - \frac{\partial H_y}{\partial z} - \sigma E_x \right) \quad (2.2.4)$$

$$\frac{\partial E_y}{\partial t} = \frac{1}{\epsilon} \left( \frac{\partial H_x}{\partial z} - \frac{\partial H_z}{\partial x} - \sigma E_y \right) \quad (2.2.5)$$

$$\frac{\partial E_z}{\partial t} = \frac{1}{\epsilon} \left( \frac{\partial H_y}{\partial x} - \frac{\partial H_x}{\partial y} - \sigma E_z \right) \quad (2.2.6)$$

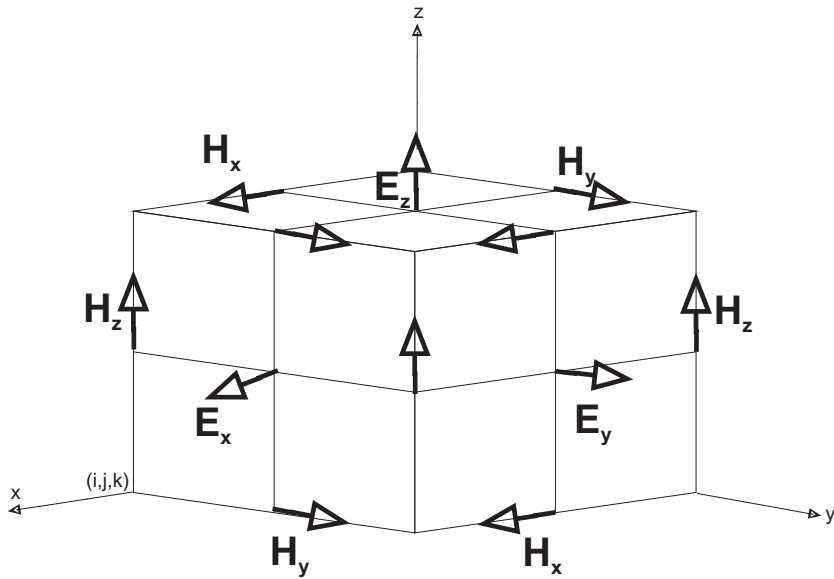


Figure 2.2.1: The Yee cell at index  $(i,j,k)$ .

The time stepping is showed in Figure 2.2.2 which explains how the time steps and the spatial steps relate to each other. The FDTD method is expressed as a continuous method and the function is discretised as central differences.

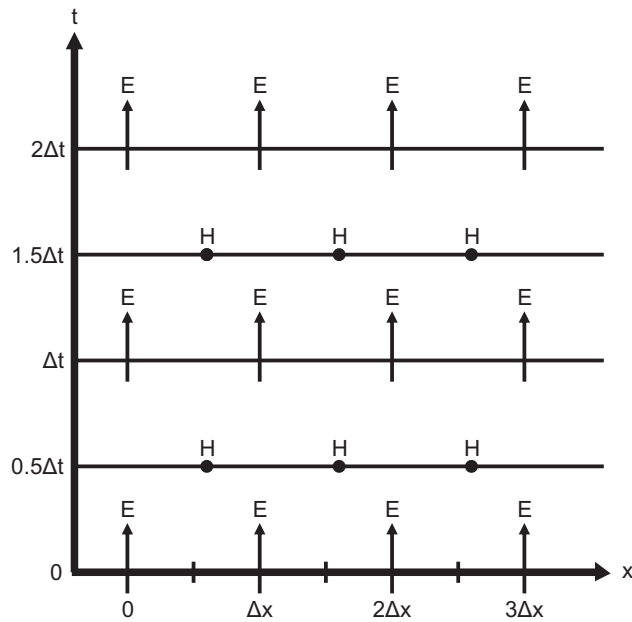


Figure 2.2.2: The FDTD time stepping.

### 2.2.1 Discretisation

The discretisation is performed by first labelling each grid cell according to the size of the grid cell and then according to the right time step. The time step is a derived parameter from the simulation time which is chosen so that the signals can propagate through all the grid cells and die out in the absorbing boundary. The index of one grid cell can be denoted as  $(i, j, k)$  and the size in all three directions are  $\Delta x$ ,  $\Delta y$  and  $\Delta z$ . This gives a denotation for the function  $F$  as

$$F_{i,j,k}^n = F(i\Delta x, j\Delta y, k\Delta z) \quad (2.2.7)$$

where  $n$  is the  $n$ th time step in the iteration process. Now the Equation 2.2.1 can be discretised as

$$\frac{H_x|_{i,j,k}^{n+\frac{1}{2}} - H_x|_{i,j,k}^{n-\frac{1}{2}}}{\Delta t} = \frac{1}{\mu_{i,j,k}} \left( \frac{E_y|_{i,j,k+\frac{1}{2}}^n - E_y|_{i,j,k-\frac{1}{2}}^n}{\Delta z} - \frac{E_z|_{i,j+\frac{1}{2},k}^n - E_z|_{i,j-\frac{1}{2},k}^n}{\Delta y} \right) \quad (2.2.8)$$

and the Equations 2.2.2 - 2.2.6 are discretised the same way. The time step,  $\Delta t$ , must fulfil a certain criteria to make the solution numerical stable [8].

$$\Delta t \leq \frac{1}{\sqrt{\frac{1}{(\Delta x)^2} + \frac{1}{(\Delta y)^2} + \frac{1}{(\Delta z)^2}}} \quad (2.2.9)$$

If the spatial steps are chosen to be equal, i.e.  $\Delta x = \Delta y = \Delta z = \Delta$ , then the time step must be chosen to:

$$\Delta t \leq \frac{\Delta}{c\sqrt{3}} \quad (2.2.10)$$

## 2.3 Electromagnetic source

In FDTD simulations there is a need for having accurate models for the physical electromagnetic source. The positions as well as the electromagnetic properties are of importance. This section covers the different ways of modelling the physical aspects of the source.

### 2.3.1 Hard source

The simplest model of the electromagnetic source is called hard source and is basically a time varied function at one of the  $\mathbf{E}$ - or  $\mathbf{H}$ -components positioned in the FDTD grid [9]. The function used is a sinusoidal wave which is

independent of the placement of the function in the spatial domain, however the time step is used to calculate the source of the wave. In a one dimensional grid at point  $k$  the  $E_z$ -component is the wave source with frequency  $f_0$  which is valid from  $n = 0$ .

$$E_z^n = E_0 \sin(2\pi f_0 n \Delta t) \quad (2.3.1)$$

The main disadvantage of this source model is that when the wave propagates through a material there will be a reflection and a transmission. The reflection will after a finite number of time steps,  $\Delta t$ , reach the source point where the grid cell assigned to the source cannot be changed. This gives a reflection as the failure to update a point must give a reflection so that the energy from the wave is not destroyed.

In two- and three-dimensional FDTD simulations the wave is cylindrical respective spherical thus making the reflection effect less important. This is because in the one dimensional case the wave propagation are aligned at one axis and therefore the reflections must be aligned to the same axis.

### 2.3.2 Resistive voltage source

The resistive voltage source is an extension of the hard source which eliminates the problem with the reflected wave at the source point. The source is modelled as a coaxial cable with specified impedance connected to the active antenna which consists of a solid wire with or without insulation. There is a need of having a model of a resistor to be able to include the resistance into the voltage source. This is achieved by adding a current density term  $\mathbf{J}_L$  in Equation 2.1.4. The current density when the source is aligned in z-direction is given by

$$\mathbf{J}_L = \frac{\mathbf{I}_L}{\Delta x \Delta y} \quad (2.3.2)$$

where

$$\mathbf{I}_L = \frac{\Delta z}{R_S} \frac{\partial \mathbf{E}}{\partial t} \quad (2.3.3)$$

which results in

$$\nabla \times \mathbf{H} = \mathbf{J}_e + \frac{\partial \mathbf{D}}{\partial t} + \frac{\mathbf{I}_L}{\Delta x \Delta y} + \frac{\mathbf{V}}{R_S} \quad (2.3.4)$$

where the added term  $\frac{\mathbf{V}}{R_S}$  is representing the voltage source. Now Equation 2.1.5 is used and the time derivative of the electric field is isolated and

discretised as

$$\begin{aligned}
 E_z|_{i,j,k}^{n+1} = & \left( \frac{1 - \frac{\Delta t \Delta z}{2R_S \epsilon_0 \Delta x \Delta y}}{1 + \frac{\Delta t \Delta z}{2R_S \epsilon_0 \Delta x \Delta y}} \right) E_z|_{i,j,k}^n + \left( \frac{\frac{\Delta t}{\epsilon_0}}{1 + \frac{\Delta t \Delta z}{2R_S \epsilon_0 \Delta x \Delta y}} \right) (\nabla \times \mathbf{H})_z|_{i,j,k}^{n+1/2} \\
 & + \left( \frac{\frac{\Delta t}{R_S \epsilon_0 \Delta x \Delta y}}{1 + \frac{\Delta t \Delta z}{2R_S \epsilon_0 \Delta x \Delta y}} \right) V_S^{n+1/2}
 \end{aligned} \tag{2.3.5}$$

where  $R_S$  is the feed resistance.

### 2.3.3 Thin wire

The active antennas are modelled as a thin wire, i.e. a fraction of the grid cell, consisting of a Perfect Electric Conductor (PEC) which corresponds to an  $\mathbf{E}$ -field with all tangential components set to zero. In reality the metal wire is a PEC which is modelled as setting the  $\mathbf{E}$ -field components that corresponds to the metal surface to zero. This will give the boundary condition that no electric field is present on the metal wire's surface. The wire carries a current and thus the surrounding  $\mathbf{H}$ -components are affected. All the  $\mathbf{H}$ -components vary by  $1/r$  where  $r$  is the distance to the wire and the axial  $\mathbf{E}$ -components that are aligned with the antenna are set to zero [9, 10, 11].

## 2.4 Absorbing boundary conditions

There is a need for a limitation of the simulated FDTD space as an endless space is impossible to cover in the simulation. If a wave is propagating to one of the walls of the simulation space there will be an unwanted reflection as the central differences cannot be calculated in the end of the simulation region. That is why an Absorbing Boundary Condition (ABC) needs to be defined making all the waves that is propagating to the outside of the computational domain to be eliminated. Another solution is to make the computational domain significantly larger so that the time the wave is travelling towards the wall is longer than the simulation time. However this will give an unnecessary large domain hence the memory and the processor cycles used for the computation will be higher as well as the total simulation time.

One of the two main types used is analytical absorbing boundary conditions which alters the computational equations in a layer situated on the outside of the original computational domain. When using this strategy

the plane waves are effectively damped as long as they are propagating perpendicular, when not there will be a reflection proportional to the angle of incidence.

The other major ABC consists of an absorbing material that is effectively damping a perpendicular wave [12]. Berenger introduced the term Perfect Matched Layer (PML) which is his name for the invented material that absorbs all incident waves of all frequencies and polarisations [13]. This was achieved by splitting the  $\mathbf{H}$ - and  $\mathbf{E}$ -components in two orthogonal components inside the absorbing boundary layer and formulating the differential equations similar to Equations 2.2.1 - 2.2.6 with material properties of a dispersion-less medium. Berenger only consider this method for the two dimensional FDTD grid, so Katz *et al.* extended the PML to three dimensions [14].

There is a more developed ABC called Convolutional PML (CPML) which absorbs outgoing waves even better. The CPML is based on a coordinate space stretch where Ampere's law is specified in the x-projection as follows

$$j\omega\epsilon E_x + \sigma E_x = \frac{1}{s_y} \frac{\partial}{\partial y} H_z - \frac{1}{s_z} \frac{\partial}{\partial z} H_y \quad (2.4.1)$$

where  $s_i$  denotes the stretched coordinate metrics which is given by

$$s_i = 1 + \frac{\sigma_i}{j\omega\epsilon_0} \quad (2.4.2)$$

where the index  $i$  denotes the  $x$ -,  $y$ - or  $z$ -coordinate. The next step is to transform Equation 2.1.4 into the time domain. There will be a convolution during the transformation thus the name convolutional PML

$$\epsilon \frac{\partial}{\partial t} E_x + \sigma E_x = \bar{s}_y(t) * \frac{\partial}{\partial y} H_z - \bar{s}_z(t) * \frac{\partial}{\partial z} H_y \quad (2.4.3)$$

where  $\bar{s}_i(t)$  is  $s_i^{-1}$  after inverse Laplace transform. In this form the CPML is time continuous so there is a need for a discretisation.

The discretisation is performed by first assuming that

$$s_i = \kappa_i + \frac{\sigma_i}{\alpha_i + j\omega\epsilon_0} \quad (2.4.4)$$

where  $\alpha_i$  and  $\sigma_i$  are positive real numbers and  $\kappa_i \geq 1$ . Furthermore assuming that  $\bar{s}_i = s_i^{-1}$  gives the impulse response for  $\bar{s}_i$  as follows

$$\bar{s}_i(t) = \frac{\delta(t)}{\kappa_i} - \frac{\sigma}{\epsilon_0 \kappa_i^2} \exp\left(-\left(\frac{\sigma_i}{\epsilon_0 \kappa_i} + \frac{\alpha_i}{\epsilon_0}\right)t\right) u(t) = \frac{\delta(t)}{\kappa_i} + \varsigma_i(t) \quad (2.4.5)$$

## 2. THE FDTD METHOD

---

where  $\delta(t)$  is the Dirac delta function and  $u(t)$  is the unit step function. Now  $\bar{s}_i$  can be inserted into 2.4.3 which gives

$$\begin{aligned} \epsilon_r \epsilon_0 \frac{\partial}{\partial t} E_x + \sigma E_x &= \frac{1}{\kappa_y} \frac{\partial}{\partial y} H_z - \frac{1}{\kappa_z} \frac{\partial}{\partial z} H_y \\ &+ \varsigma_y(t) * \frac{\partial}{\partial y} H_z - \varsigma_z(t) * \frac{1}{\kappa_z} \frac{\partial}{\partial z} H_y \end{aligned} \quad (2.4.6)$$

The discrete impulse response of  $\varsigma_i(t)$  is defined below as

$$\begin{aligned} Z_i(m) &= \int_{m\Delta t}^{(m+1)\Delta t} \varsigma_i(\tau) d\tau \\ &= -\frac{\sigma_i}{\epsilon_0 \kappa_i^2} \int_{m\Delta t}^{(m+1)\Delta t} \exp\left(-\left(\frac{\sigma_i}{\epsilon_0 \kappa_i} + \frac{\alpha_i}{\epsilon_0}\right)\tau\right) d\tau \\ &= a_i \exp\left(-\frac{\sigma_i}{\kappa_i} + \alpha\right) \frac{m\Delta t}{\epsilon_0} \end{aligned} \quad (2.4.7)$$

where

$$a_i = \frac{\sigma_i}{\sigma_k \kappa_i + \kappa_i^2 \alpha_i} \left[ \exp\left(-\left(\frac{\sigma_i}{\kappa_i} + \alpha_i\right) \frac{\Delta t}{\epsilon_0}\right) - 1.0 \right] \quad (2.4.8)$$

Now can Equation 2.4.6 be discretised according to the Yee scheme by inserting Equation 2.4.7 and 2.4.8 as follows

$$\begin{aligned} \epsilon_r \epsilon_0 \frac{E_x|_{i+1/2,j,k}^{n+1} - E_x|_{i+1/2,j,k}^n}{\Delta t} + \sigma \frac{E_x|_{i+1/2,j,k}^{n+1} - E_x|_{i+1/2,j,k}^n}{2} \\ &= \frac{H_z|_{i+1/2,j+1/2,k}^{n+1/2} - H_z|_{i+1/2,j-1/2,k}^{n+1/2}}{\kappa_y \Delta y} \\ &\quad - \frac{H_y|_{i+1/2,j,k+1/2}^{n+1/2} - H_y|_{i+1/2,j,k-1/2}^{n+1/2}}{\kappa_z \Delta z} \\ &\quad + \sum_{m=0}^{N-1} Z_{0_y}(m) \frac{H_z|_{i+1/2,j+1/2,k}^{n-m+1/2} - H_z|_{i+1/2,j-1/2,k}^{n-m+1/2}}{\Delta y} \\ &\quad - \sum_{m=0}^{N-1} Z_{0_z}(m) \frac{H_y|_{i+1/2,j,k+1/2}^{n-m+1/2} - H_y|_{i+1/2,j,k-1/2}^{n-m+1/2}}{\Delta z} \end{aligned} \quad (2.4.9)$$

The convolution in Equation 2.4.9 can efficiently be achieved with the recursive convolution method [9, 15, 16].

# Chapter 3

## Reconstruction of dielectric properties

The idea behind the reconstruction is the essential part of the microwave tomography as the measurements itself do not give any information if there is a tumour in the examined breast. The measured data must be processed so that the dielectric properties can be obtained.

### 3.1 Dielectric properties of human tissues

In microwave tomography the dielectric properties of human tissues are of interest as the resulting images consist of the reconstructed permittivity and conductivity. The reason of interest is that the contrast between healthy tissue and tumours are large and this can be used to discriminating between healthy tissue and tumours. Secondly, when using a broadband signal the dispersive response to the microwaves, i.e. the permittivity and conductivity changes with different frequencies, of the human tissue can be used to detect tumours as there is a different frequency response for tumours and healthy tissue.

#### 3.1.1 Dispersive response

The human tissues show a dispersive response, i.e. frequency dependence, when exposed to an electric field. The dispersive response is mainly cause by the cell membrane in lower frequency ranges and in higher the water molecules in the tissue cause the dispersive response [17].

#### $\alpha$ -dispersion

The  $\alpha$ -dispersion corresponds to the frequency region of  $<1$  kHz where the permittivity is very high. The mechanism behind the dispersion is the diffusion of ions in and out through the cell membrane which consists of a phospholipid bilayer. Each of these phospholipids is aligned with the hydrophobic lipid against each other, forming a layer in between filled with proteins. In between these layers are ports allowing ions to move in or out by preserving an electric potential of 70 mV, due to the small thickness of the membrane, typically 7 nm, the electric field will be high, typically 10 MV/m. Organelles that resides inside the cell can affect the  $\alpha$ -dispersion by different charges as well as the impedance of the membrane.

#### $\beta$ -dispersion

The  $\beta$ -dispersion is situated in a frequency region of 10 kHz - 10 MHz and is caused by the capacitive charging in the cellular membranes and the intracellular bodies bounded to the membrane. This is often referred to as interfacial polarisation.

#### $\gamma$ -dispersion

The  $\gamma$ -dispersion occurs in a frequency region of  $> 100$  MHz and is due to movement of free dipoles, i.e. water molecules. The water molecules that are bounded show a different frequency response proportional to the water content in the tissue.

### 3.1.2 Relaxation process

The dispersive response of the human tissue when applying an electrical field is not instantaneous so there is a need for a model of how the dielectric properties vary. A model that includes this was made by Debye and can be extended with a static conductivity to include ion drifts as follows

$$\epsilon^*(\omega) = \epsilon_\infty + \frac{\epsilon_{static} - \epsilon_\infty}{1 + j\omega\tau_n} + \frac{\sigma_{static}}{j\omega\tau} \quad (3.1.1)$$

In human tissue there is often more than one relaxation frequency and Cole & Cole formulated a model to compensate for this in [18, 19].

$$\epsilon^*(\omega) = \epsilon_\infty + \sum_n \frac{\Delta\epsilon_n}{1 + (j\omega\tau_n)^{1-\alpha_n}} + \frac{\sigma_{static}}{j\omega\epsilon_0} \quad (3.1.2)$$

This model needs parameters that are obtained by measuring and fitting of the data.

## 3.2 Measure procedure

The measurements are performed with a vector network analyser of make and model Agilent E8362 B. This is a two port device which is used to send a signal on one of the ports and receive on the other one. The signal consist of a wave that is either transmitted,  $a$ , from one port to the other one or reflected,  $b$ , to the first. This process results in a unit less transmission coefficient which is denoted  $S_{21}$ . The first port is also receiving when the signal has been sent and this gives the reflection coefficient  $S_{11}$ . This procedure is repeated for the second port and then the  $S_{12}$  and  $S_{22}$  coefficients are achieved. The four different scattering parameters can be denoted as [20]:

$$S_{11} = \left. \frac{b_1}{a_1} \right|_{a_2=0} ; S_{21} = \left. \frac{b_2}{a_1} \right|_{a_2=0} \quad (3.2.1)$$

$$S_{12} = \left. \frac{b_1}{a_2} \right|_{a_1=0} ; S_{22} = \left. \frac{b_2}{a_2} \right|_{a_1=0} \quad (3.2.2)$$

where  $a_1$ ,  $a_2$ ,  $b_1$  and  $b_2$  are the waves described in Figure 3.2.1.

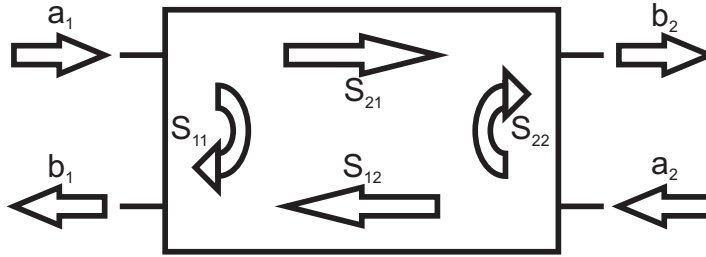


Figure 3.2.1: The scattering parameters for a two port network analyser.

The measurement described above is however not satisfying as there is only two ports and thus there can be only two antennas. The solution to this is connecting a multiplexer with 2:32 ports, namely a Cytec CXM/128-S-W, which can be controlled by a computer. The antenna array consists of 32 antennas placed in four different rings each shifted 22.5 degrees with eighth antennas in each, all of them placed inside a cylinder made of acrylic, see Figure 3.2.2.

The measurements are made in the frequency domain and the FDTD method is in the time domain so there is a need for a transformation which is done by taking the inverse Fourier transform of the coefficients respectively. The data is already in discrete form so there is no need for discretisation before the transformation.

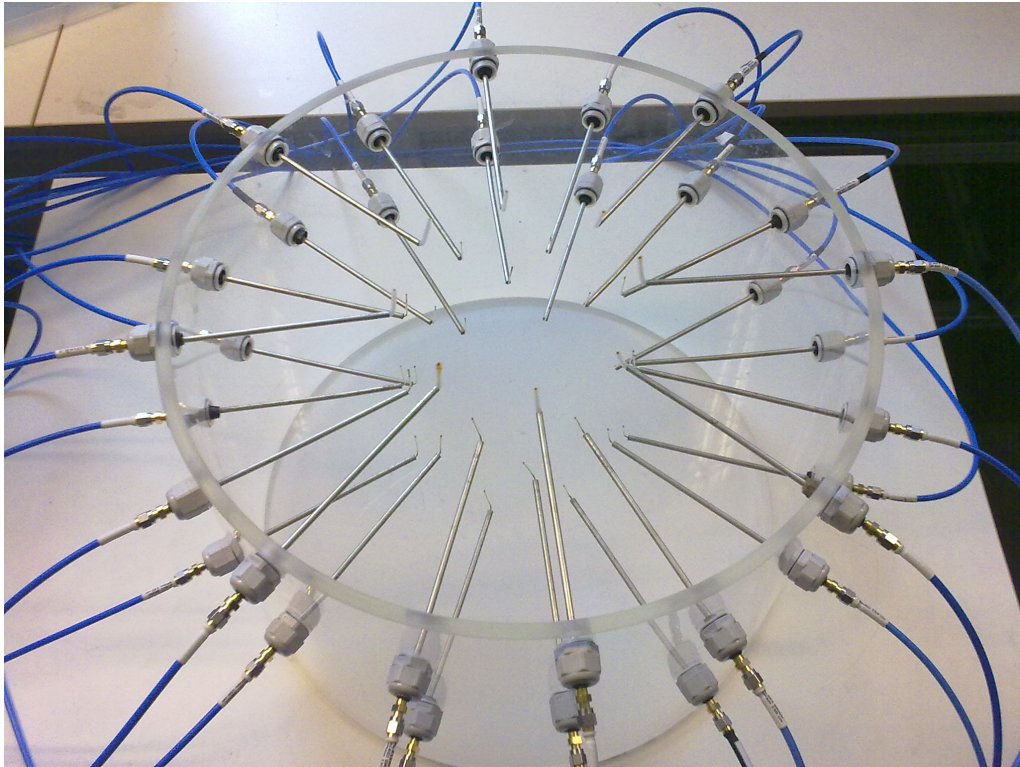


Figure 3.2.2: A photo of the antenna array.

### 3.3 The reconstruction algorithm

In this work the reconstruction of the dielectric properties is made in the same way as in Fhager 2006 [10] with adaption to three dimensions and convolutional perfect matched layer as absorbing boundary condition in the FDTD simulator. The software used is the same as described in Fhager et al. 2010 [21].

The reconstruction is performed by minimising a cost functional that is given by the measurements compared to several simulated electric fields with different dielectric properties between source and receiver. When the difference between the simulation and the measurement are small enough the minimisation stops and the dielectric properties are updated. This procedure is repeated for all FDTD grid cell in a predefined reconstruction region which is preferable slightly larger than the object that is measured.

There is a starting criterion where all of the grid cells are assigned uniform background properties which will not change if not updated by the

algorithm. Also there is no reconstruction of the permeability as biological tissue is often not magnetic.

Calibration of the measurement is important as the cables and the multiplexer have frequency properties that can introduce disturbances. The calibration is performed with an electric calibrator with two of the antenna cables mounted in the array removed and connected to the calibrator. However this will not calibrate the differences in the antennas nor the slightly difference in the cables so there is a need for another calibration. The second calibration is performed by measuring on an empty system and that information is later used in the reconstruction.

In the reconstruction process the simulated electrical field is calibrated with the measured scattering parameters as

$$E_{cal}^{meas}(f) = \frac{S_{scat}^{meas}(f)}{S_{ref}^{meas}(f)} E_{ref}^{sim}(f) \quad (3.3.1)$$

where  $S_{scat}^{meas}$  denotes the measured transmission or reflection coefficient for the antenna pair used in the measurement performed on an object. The reference scattering data,  $S_{ref}^{meas}$ , is measured without an object in the antenna array and the resulting  $E_{cal}^{meas}(f)$  is now considered as the electric field at the antenna used as a receiver.  $E_{ref}^{sim}(f)$  denotes the simulated electric field and is given by the Fourier transform of a Gaussian pulse

$$E_{ref}^{sim}(t) = E_0 \exp\left(-\frac{1}{2} \frac{(t - t_1)^2}{t_0^2}\right) \sin(\omega t) \quad (3.3.2)$$

with pulse width  $t_0$  and  $t_1 = 4t_0$ .

The reconstruction is performed by minimisation of an introduced functional

$$F(\boldsymbol{\epsilon}, \boldsymbol{\sigma}) = \int_0^T \sum_{m=1}^M \sum_{n=1}^N \left| \mathbf{E}_{mn}^{sim}(\boldsymbol{\epsilon}, \boldsymbol{\sigma}, t) - \mathbf{E}_{mn}^{meas}(t) \right|^2 dt \quad (3.3.3)$$

where  $\mathbf{E}_{mn}^{meas}(\boldsymbol{\epsilon}, \boldsymbol{\sigma}, t)$  is a time varying electric field, from antenna number  $m$  to antenna number  $n$ , obtained by taking the inverse Fourier transform of the calibrated measurement electric field,  $E_{cal}^{meas}(f)$ . The field  $\mathbf{E}_{mn}^{sim}(\boldsymbol{\epsilon}, \boldsymbol{\sigma}, t)$  is obtained by several different simulations with varying permittivity and conductivity.

The minimisation is achieved with a conjugate-gradient algorithm where the gradients are derived by increasing the dielectric properties, i.e.  $\boldsymbol{\epsilon} + \delta\boldsymbol{\epsilon}$  and  $\boldsymbol{\sigma} + \delta\boldsymbol{\sigma}$ , and a change in the functional is then derived with perturbation. Now the functional can be expressed as a Fréchet derivative as

$$F'(\boldsymbol{\epsilon}, \boldsymbol{\sigma}) = \langle G_{\boldsymbol{\epsilon}}(\mathbf{x}), \delta\boldsymbol{\epsilon}(\mathbf{x}) \rangle + \langle G_{\boldsymbol{\sigma}/\langle\boldsymbol{\sigma}\rangle}(\mathbf{x}), \delta\boldsymbol{\sigma}(\mathbf{x}) \rangle \quad (3.3.4)$$

### 3. RECONSTRUCTION OF DIELECTRIC PROPERTIES

---

where the surface integral for the reconstruction domain defines the inner product as

$$\langle G_i(\mathbf{x}), \delta i(\mathbf{x}) \rangle = \iiint_V G_i(\mathbf{x}) \delta i(\mathbf{x}) dV \quad (3.3.5)$$

When formulating the gradients the difference between the simulated and the measured fields are used as sources in the adjoint Maxwell's equations. The two gradients are defined for the two dielectric properties in all grid cells for a given reconstruction domain as follows

$$G_\epsilon(\mathbf{x}) = 2 \sum_{m=1}^M \int_0^T \tilde{\mathbf{E}}_m(\epsilon, \sigma, \mathbf{x}, t) \cdot \partial_t \mathbf{E}_m(\epsilon, \sigma, \mathbf{x}, t) dt \quad (3.3.6)$$

$$G_{\sigma/\langle\sigma\rangle}(\mathbf{x}) = 2 \langle\sigma\rangle \sum_{m=1}^M \int_0^T \tilde{\mathbf{E}}_m(\epsilon, \sigma, \mathbf{x}, t) \cdot \mathbf{E}_m(\epsilon, \sigma, \mathbf{x}, t) dt \quad (3.3.7)$$

In both gradients  $\tilde{\mathbf{E}}_m(\epsilon, \sigma, \mathbf{x}, t)$  is the simulated  $\mathbf{E}$ -field in the reconstruction domain, and  $\mathbf{E}_m(\epsilon, \sigma, \mathbf{x}, t)$  is calculated from the adjoint Maxwell's equations with the difference between the simulated and the measured fields when antenna  $m$  is the source. There is also a scale component,  $\langle\sigma\rangle$ , that is compensating for different scaling in the gradients as

$$\langle\sigma\rangle = \left( \int_0^\infty |\hat{\mathbf{E}}_{mn}(\omega)|^2 d\omega \right)^{-1} \times \int_0^\infty |\hat{\mathbf{E}}_{mn}(\omega)|^2 \omega d\omega \quad (3.3.8)$$

here the antenna number  $m$  transmits and antenna  $n$  receives an electrical field.  $\hat{\mathbf{E}}_{mn}(\omega)$  is the Fourier transformation of this measured time domain  $\mathbf{E}$ -field. The reconstruction procedure is severely affected by the choice of the scaling parameter  $\langle\sigma\rangle$ .

The meaning of introducing the gradients is to minimise the functional which is achieved by following the gradient in the negative direction. This is known as line searching and can be performed in several different ways, here parabolic interpolation is used. There will be two different gradients for each FDTD grid cell as there is two different dielectric properties to reconstruct, however the computation of the gradients involves several different FDTD simulations with varying permittivity and conductivity in the same grid cell which is very time consuming. This is repeated until the accuracy is satisfying [10, 21].

# Chapter 4

## Modelling of the antenna array

Dipoles are one of the simplest antenna types. The dipoles can have one of the poles substituted with a ground plane and is then known as a monopole [22]. In this thesis monopoles have been used to great extent as they are easier to model and manufacture. However there is no ground plane in this setup so the antennas must be modelled in a slightly different way. There is also an effect of the cables that needs to be taking into account when modelling the antenna as the cables are made of metal. Furthermore some of the antennas in the array are aligned in an angle towards the FDTD grid axes and this effect is also investigated. Finally the FDTD model of the antenna array is compared to the measured data obtained from the resulting antenna array.

### 4.1 Antennas in an infinite large water tank

This simulation was done with water as a lossy medium, the background relative permittivity is 78 and the background conductivity is set to 0.2 S/m. The reason for having a lossy medium is that the currents running in the outer conductor is attenuated and these currents are difficult to include in a model. The antenna is modelled in several different ways to see if the effect of the cable can be disregarded.

#### 4.1.1 Length and frequency

The length of the antenna is determined by the wanted resonance frequency. This frequency should preferably be in the range where the measurements shall be made. The measurement frequency must be in a range where a suspected tumour has different dielectric properties than the rest of the

examined part. This gives that the antennas system should be able to measure at several different frequencies typically in the range of 300 MHz to 2 GHz. The antenna length,  $l$ , is calculated for a quarter-wave monopole as

$$l = \frac{\lambda}{4} \quad (4.1.1)$$

where

$$\lambda = \frac{v_p}{f_r} \quad (4.1.2)$$

where  $f_r$  is the resonance frequency and  $v_p$  is the phase speed in the medium surrounding the antenna which is given by

$$v_p = \frac{c}{\sqrt{\epsilon_r}} \quad (4.1.3)$$

where  $c$  is the speed of light in vacuum and  $\epsilon_r$  is the relative permittivity for the surrounding medium [23]. The chosen length was 10 mm and frequency 1.3 GHz for the antenna which can be seen in Figure 4.1.2.

#### 4.1.2 Evaluation of different antennas in water

The reason for modelling the cables is to investigate if the effect can be neglected as the reconstruction process requires an accurate model of the antenna array. When the effect of the cable is low the model of the whole antenna and cable can be simplified to just include the antenna itself which is an advantage because the simulation domain can be made smaller without losing accuracy. A smaller domain will decrease the memory and time consumption which is advantageous. The antennas are simulated in a tank aligned symmetrically with the x-coordinate axle 80 mm apart and the end of the cable towards the end of the simulation domain. Outside of the simulation domain there is a CPML absorbing all outgoing waves so there is no reflection from a wall, this is covered later on. The antennas can be simulated without any connector, however in reality there is no way of measuring without having a cable connecting the antenna with the measuring equipment. The cables are also used to fixate the antennas in the array as they are made very stiff.

The antennas radiate the waves in a radial symmetry and are therefore aligned so that the inner conductors are pointing in z-direction and the cables are aligned in the xy-plane. This gives that the cables, the outer conductor, or the inner conductor must be bent in some way. There is several different ways to bend the outer conductor and this section cover simulations of five different cases compared to an antenna without any

connector modelled as illustrated in Figure 4.1.1. These different ways of bending the conductors are illustrated in Figure 4.1.3 and Figure 4.1.7. The FDTD model used for the antennas is the thin wire approximation, described in Section 2.3.3. For simplicity the surrounding  $\mathbf{H}$ -components have been left out in the FDTD model illustrations in this chapter.

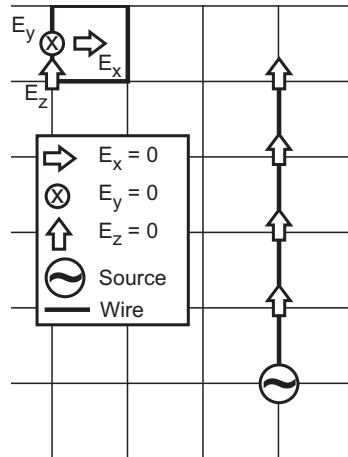


Figure 4.1.1: The FDTD model of the antenna without any cable.

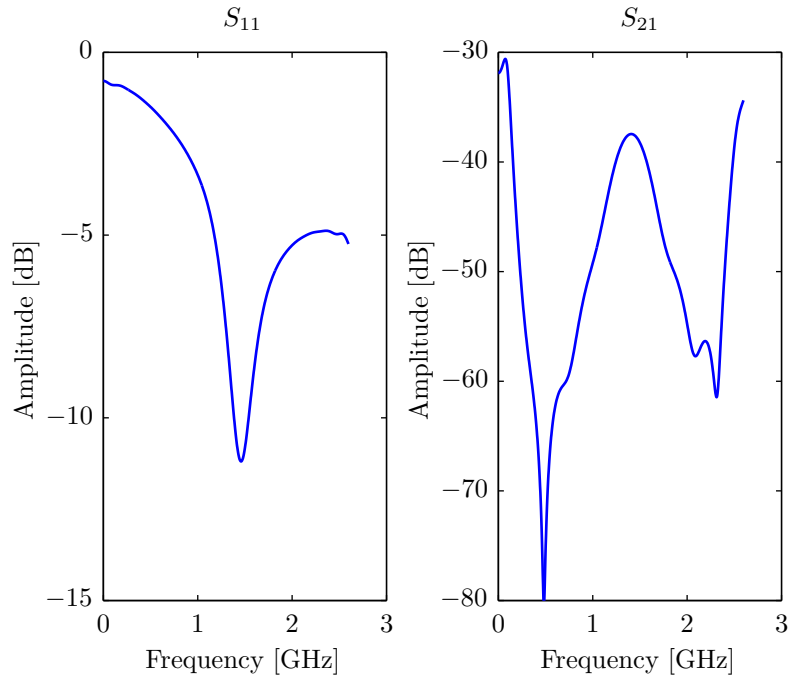


Figure 4.1.2: Reflection-,  $S_{11}$ , and transmission-coefficient,  $S_{21}$ , for the antenna shown in Figure 4.1.1.

In Figure 4.1.2 the best possible antenna with given properties is shown, however this is without any effect of the cables and the wall of the measuring tank which in reality will give a different curve. These curves are just for reference in the evaluation of which method of bending the cables is the best. The  $S_{11}$  curves have a minimum at a frequency which is called the resonance frequency, this is the frequency where the antenna is working best as there is the lowest amount of reflection at said frequency. Monopole antennas with amplitude below -10 dB at the resonance frequency are considered a good antenna. In the  $S_{21}$  curves the resonance frequency is where the curve has a maximum, in the simulation a Gaussian pulse is used and this gives model errors at low and high frequencies but in the range in between the simulation is good. This is why there are peaks in the beginning and the end of the simulated frequency range and these will not show in the measurements.

### Bent inner conductor

The first way of bending the antenna was to only bend the inner conductor which in the FDTD model corresponds to putting a Perfect Electric

Conductor cylinder of radius as the cable, i.e. 1.75 mm, under the antenna. A PEC is modelled by setting the  $\mathbf{E}$ -components to zero. In Figure 4.1.4 the  $E_x$ -components below the antenna is set to zero which then gives a model of a metallic cylinder of radius 0.5 grid cells. When using a 4 mm grid cell this corresponds to a metallic cylinder with radius of 2 mm. During this simulation the grid cell was however 1 mm, giving the amount of  $\mathbf{E}$ -components to set to zero to be higher. This is illustrated in Figure 4.1.5 where an approximation of a cylinder is made by setting  $\mathbf{E}$ -components to zero in a quadratic pattern. This pattern is repeated in the x-direction for the length of the cable.

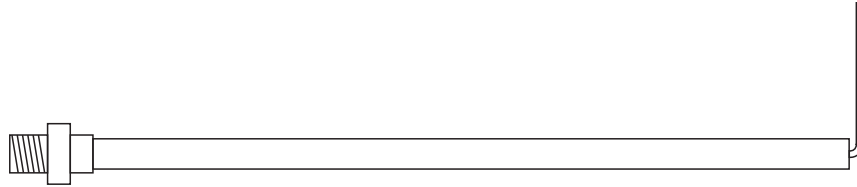


Figure 4.1.3: The antenna with only the inner conductor bent up.

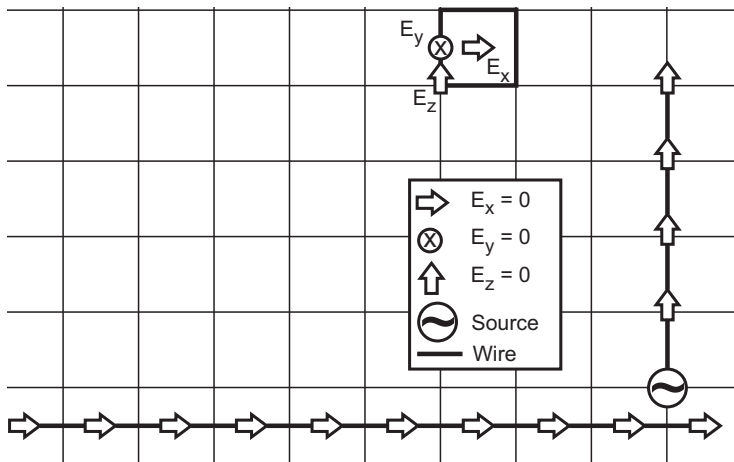


Figure 4.1.4: The FDTD model of the antenna shown in Figure 4.1.3 when using a 4 mm grid cell.

#### 4. MODELLING OF THE ANTENNA ARRAY

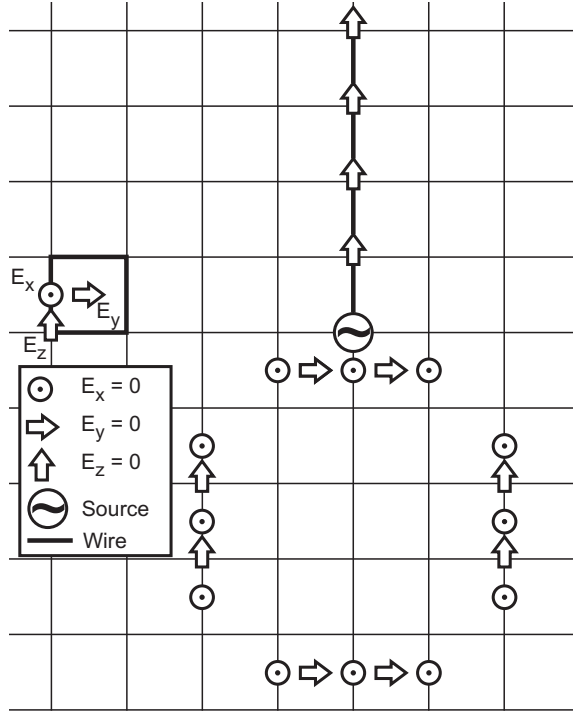


Figure 4.1.5: The FDTD model of the antenna shown in Figure 4.1.3 when using a 1 mm grid cell.

The reflection and transmission curves for this antenna model are shown in Figure 4.1.6 as well as the effect of the cable. This effect is calculated as

$$20 \log_{10} \left( \sqrt{(\Re(S_{11,cable} - S_{11,no\ cable})^2 + \Im(S_{11,cable} - S_{11,no\ cable})^2)} \right) \quad (4.1.4)$$

where  $S_{11,cable}$  is the reflection coefficient for the antenna with the cable and  $S_{11,no\ cable}$  is the reflection coefficient for the reference antenna. This is also calculated in the same way for the transmission coefficients. The cable effect is not as noticeable in the reflection coefficient as in the transmission coefficient, where the signal is lower. This gives that the effect of the cable must still be in the model, but the antenna is still working as intended i.e. the resonance frequency and the total reflection and transmission is similar.

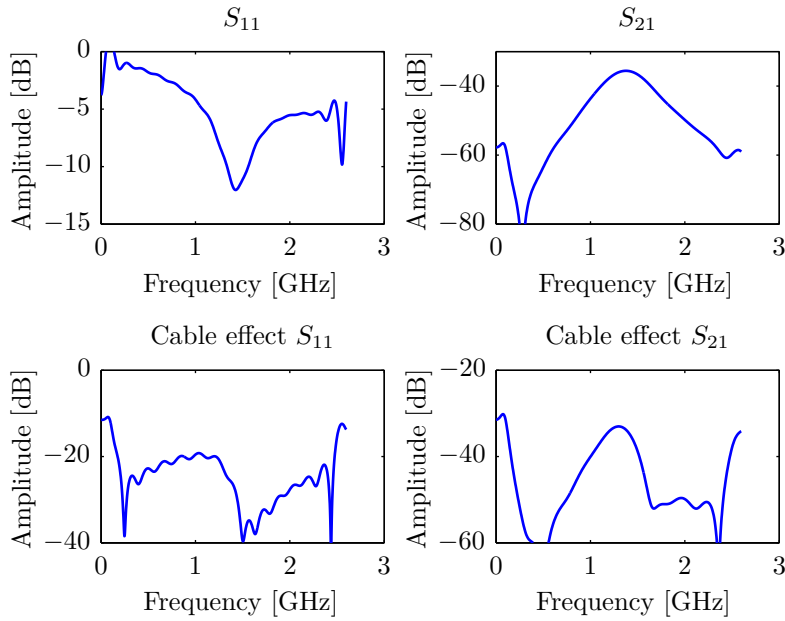


Figure 4.1.6: Reflection-,  $S_{11}$ , and transmission-coefficient,  $S_{21}$ , and the cable effect for the antenna shown in Figure 4.1.3.

### Bent outer conductor

The second way of bending the antenna was to bend the outer conductor, this was done in three ways with different length on the part that was bent i.e. 5, 10 and 15 mm. The FDTD model for these antennas is shown in Figure 4.1.8 and for simplicity the illustration shows a 4 mm grid cell with PEC cylinders with radius of 0.5 grid cells.



Figure 4.1.7: The antenna with only the outer conductor bent up.

#### 4. MODELLING OF THE ANTENNA ARRAY

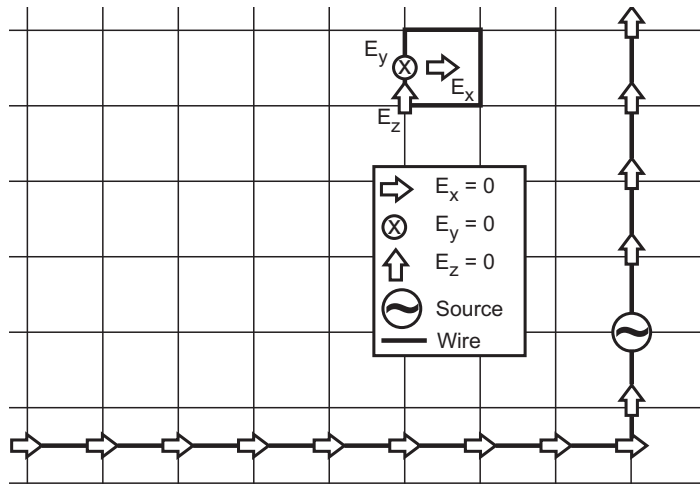


Figure 4.1.8: The FDTD model of the antenna shown in Figure 4.1.7.

This model of the antenna and the cable did not give a satisfying result as the cable effect in the reflection coefficient is too high. Furthermore the transmission coefficients for the 10 and 15 mm cases do not have a proper form, see Figure 4.1.9.

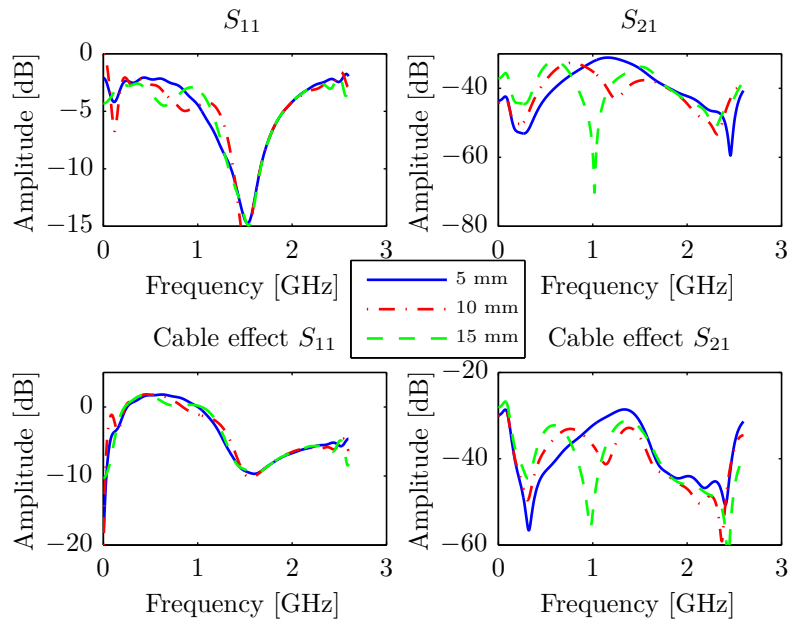


Figure 4.1.9: Reflection-,  $S_{11}$ , and transmission-coefficient,  $S_{21}$ , and the cable effect for the antenna shown in Figure 4.1.7.

### Bent inner conductor with dielectric

Another antenna was modelled with a dielectric on the inner conductor. The dielectric is modelled in the FDTD grid as setting a constant permittivity and conductivity in the grid cells closest to the inner conductor as illustrated in Figure 4.1.11. Here only the antenna with bent inner conductor was investigated as the best result was obtained this way.

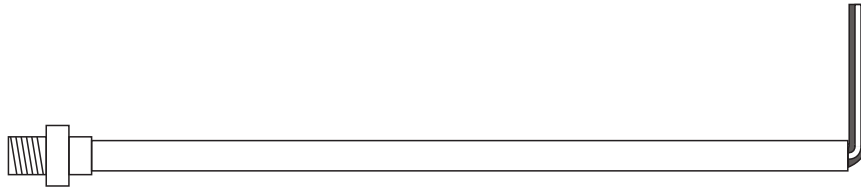


Figure 4.1.10: One antenna with dielectric.

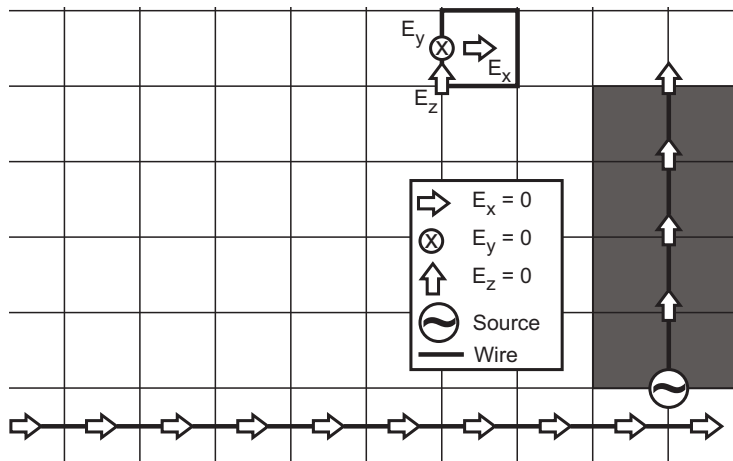


Figure 4.1.11: The FDTD model of the antenna shown in Figure 4.1.10.

#### 4. MODELLING OF THE ANTENNA ARRAY

---

When using this FDTD model the antenna showed better properties as the bandwidth is wider. This can be seen in Figure 4.1.12 as the frequency range where the antenna's reflection coefficient is low is wider as well as where the transmission coefficient is high.

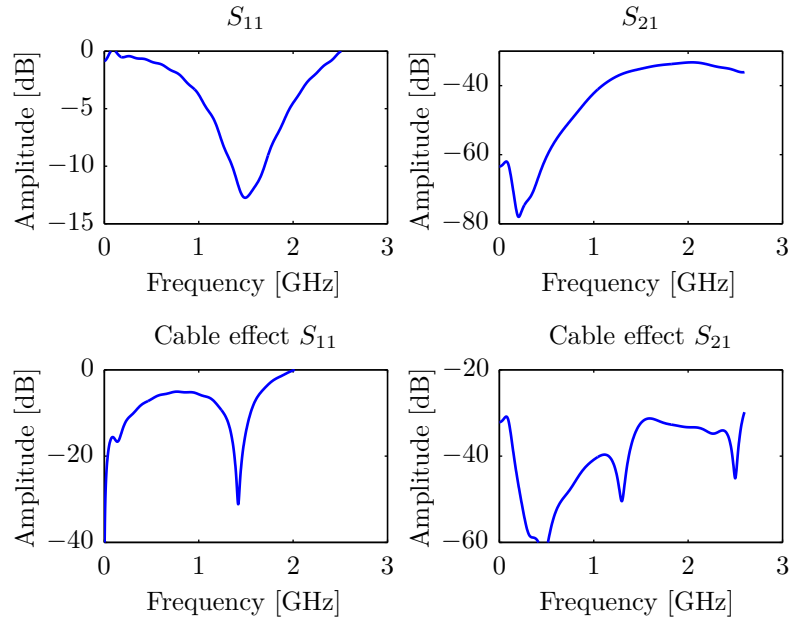


Figure 4.1.12: Reflection-,  $S_{11}$ , and transmission-coefficient,  $S_{21}$ , and the cable effect for the antenna shown in Figure 4.1.3.

This means that the antenna is working well over a wider frequency range which is a wanted property in reality as well as in the simulation. The effect of the cable and the effect of the dielectric is in this model not that interesting as the resonance frequency is shifted up in frequency. This can easily be compensated for by making the antenna slightly longer. The antenna model is however disregarded later on as the dielectric is not modelled well compared to the real antenna. The reason for this is that the grid cells cannot be made small enough to model the thickness of the dielectric as memory and time limitations occurs.

## 4.2 Modelling of the measuring tank

All simulations have been done with two antennas symmetrically placed in a water cylinder in open air with a relaxation process modelled with the Debye Equation 3.1.1. The different properties for the materials are shown in Table 4.1. The conductivity is increased in the simulated water to investigate if the edge reflections can be suppressed without increasing the tank size to much. There is trade off in the size of the tank and the increased conductivity as a too large size of the tank will increase the computation time and too large conductivity will suppress all signals. The increased conductivity is achieved by changing the  $\sigma_{static}$  in the Debye Equation 3.1.1.

	Air	Water
$\epsilon_{\infty}$	1.0	4.85
$\epsilon_{static}$	1.01	78.9
$\tau$	8.0e-12	9e-12

Table 4.1: The Debye properties of air and water.

### 4.2.1 Edge effects

One of the reasons for modelling the edge of the tank is to see if the walls must be modelled or if the simulation domain can be shrunk and thereby the memory and time consumption will be less. The other reason for investigating the edge effect is to see if a reflection going from the antenna towards the wall will cause a high enough signal to disturb the measurements. These reflections are not wanted as there is no useful information outside the measurement domain i.e. the only signals of interest are the signals reflected by an object in the measurement domain. The given reflection will depend on the object's dielectric properties which will alter the electromagnetic wave given by the transmitting antenna. The edge effects is calculated as follows

$$20 \log_{10} \left( \sqrt{(\Re(S_{11,110} - S_{11,220}))^2 + \Im(S_{11,110} - S_{11,220})^2} \right) \quad (4.2.1)$$

where  $S_{11,110}$  are the reflection coefficient for a tank where the active antenna is placed 110 mm from the wall and  $S_{11,220}$  is the reflection coefficient for a tank with the active antenna 220 mm from the wall. The reason for that the distance is 220 mm is that the tank size used for comparison must be larger, however the tank must be of a limited size. The edge effect when using water and water with increased conductivity in the tank is shown in Figure 4.2.1.

#### 4. MODELLING OF THE ANTENNA ARRAY

The simulations and measurements for two tanks with the antennas 20 mm and 55 mm from the wall are shown in the same figure. This gives an idea of how well the simulations and measurements is consistent and here the trend is right but the disturbance from the wall is higher in the measured data. The reason for not including any measurements from the larger tanks is that no big enough tank was available for the measurements.

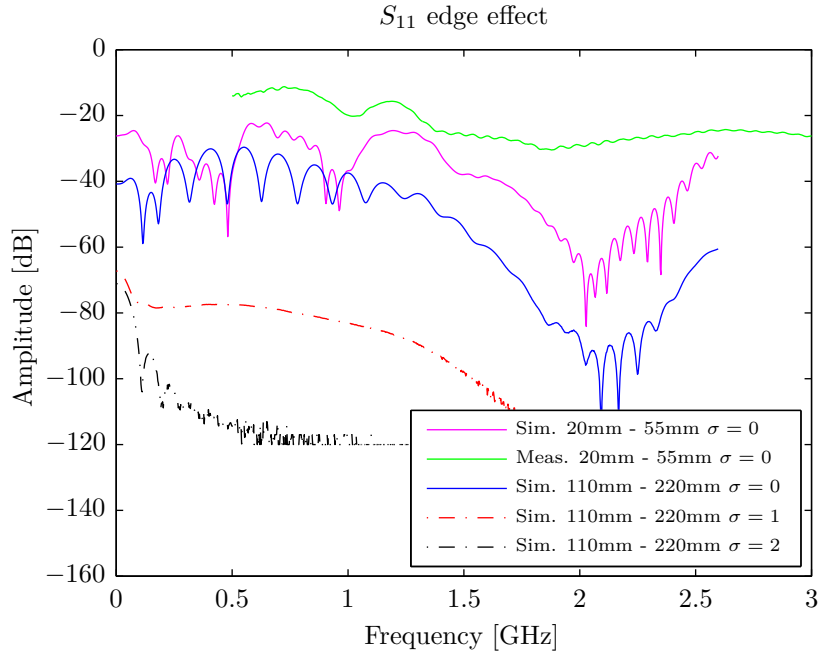


Figure 4.2.1: The edge effect for the reflection coefficient,  $S_{11}$ .

The transmitted signal is also investigated as the wall reflection could interfere with the wave the receiving antenna should receive through the measurement domain. For an antenna the transmitted signal is always lower than the reflected which makes the reflection investigation more important. The edge effect is calculated the same way as above except that the transmission coefficients,  $S_{21}$ , are used instead:

$$20 \log_{10} \left( \sqrt{(\Re(S_{21,110} - S_{21,220}))^2 + (\Im(S_{21,110} - S_{21,220}))^2} \right) \quad (4.2.2)$$

The edge effect for water and for water with increased conductivity is shown in Figure 4.2.2. Here the measurements and simulation of the smaller tank is more consistent in both trend and value.

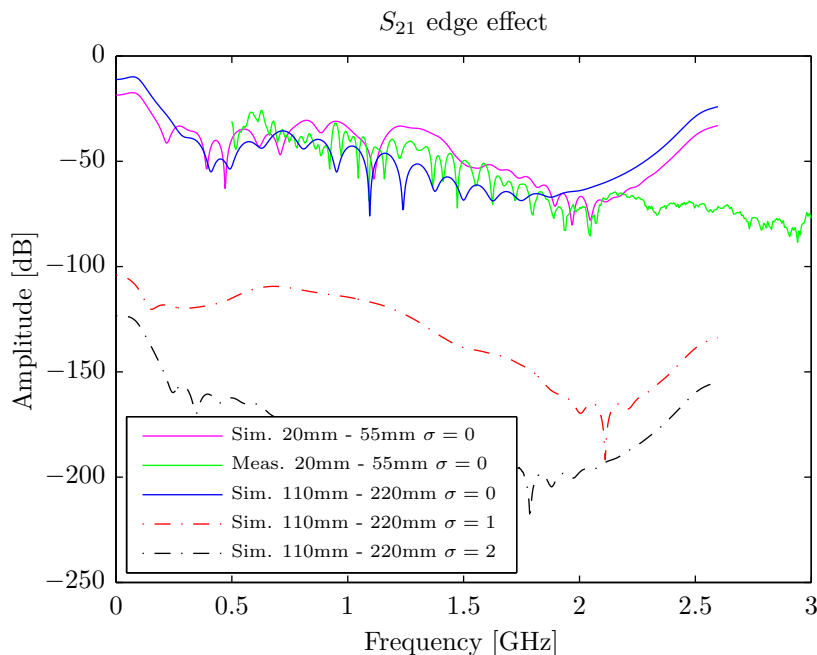


Figure 4.2.2: The edge effect for the transmission coefficient,  $S_{21}$ .

When  $\sigma_{static} = 1$  S/m the edge effect can be neglected for a tank with antennas placed 110 mm from the wall as the edge reflection is below the noise floor of -80 dB. This is a limitation in the measurement equipment and all signals below this level will be considered as noise and do not contribute to the measurements.

### 4.3 Modelling of the whole antenna array

This section covers the simulations of the complete antenna array where the FDTD grid size is set to 4 mm due to memory limitations. The tank is modelled as a water cylinder placed in open air and all the antennas have bent inner conductor which is located in circular pattern with a radius of 71 mm. The whole tank must be modelled even though effect from the edges can be neglected when using a saline solution as liquid medium. This is because the metal cables are disturbing the signals and not allowing to shrink the simulation domain.

### 4.3.1 FDTD grid coordinate axes

The FDTD grid has three coordinate axes and a placement of an antenna in any of these three directions is straightforward. When an antenna is placed in an angle towards the axes the antenna must be modelled differently. This is achieved by modelling many PEC cylinders with only one or two grid cells aligned according to the coordinate axes. In Figure 4.3.1 and Figure 4.3.2 this is illustrated for the different rings of antennas. In the first antenna ring there is eight antennas with four placed aligned with the x- and y-axis and four rotated  $45^\circ$  from the respective axes. The above antenna ring is rotated by  $22.5^\circ$  in relation to the below. This means that for this ring all the antennas are placed in an angle of  $22.5^\circ$  towards the coordinate grid axes. In Figure 4.3.3 and Figure 4.3.4 an illustration of the layout is shown.

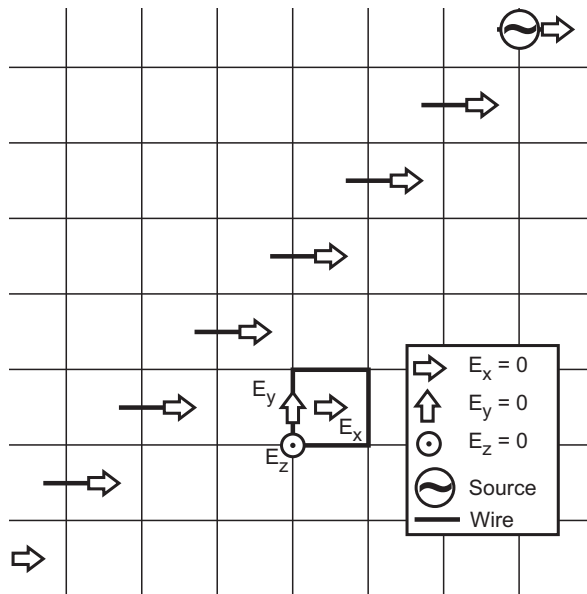


Figure 4.3.1: The FDTD model of one antenna rotated 45 degrees in relation to the FDTD coordinate axes.

### 4.3. Modelling of the whole antenna array

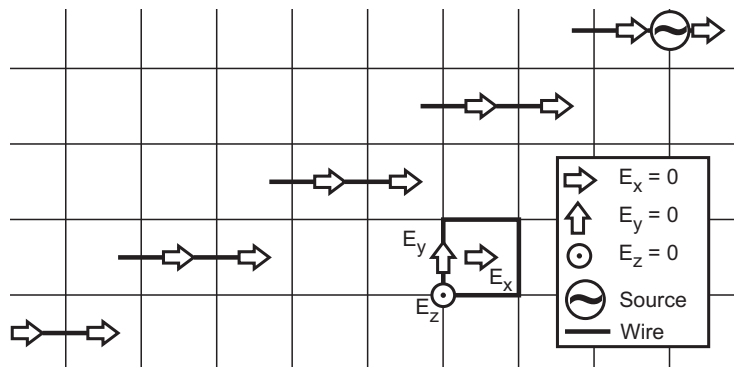


Figure 4.3.2: The FDTD model of one antenna rotated 22.5 degrees in relation to the FDTD coordinate axes.

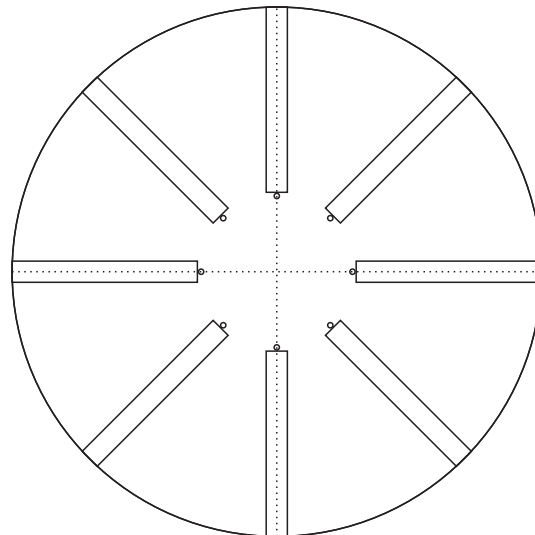


Figure 4.3.3: The layout in the xy-plane of how the antennas are placed in respect to each other when four is following the axes and four is placed in a 45° angle.

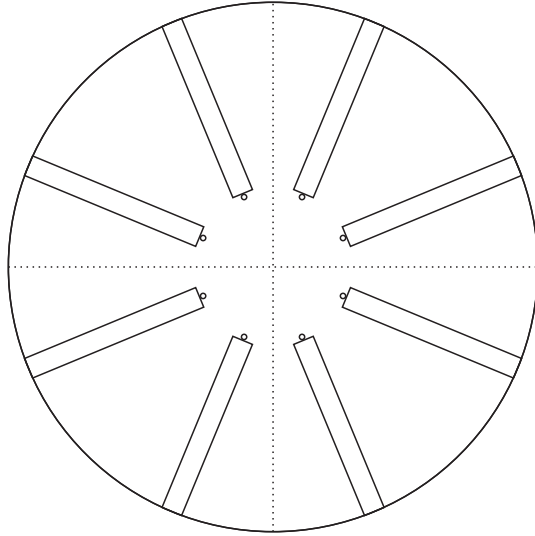


Figure 4.3.4: The layout in the  $xy$ -plane of how the antennas are placed in respect to each other when all eight is placed in a  $22.5^\circ$  angle to the coordinate axes.

The differences in the reflection- and transmission coefficient when an antenna is transmitting to an antenna placed across the measurement domain for the rotated FDTD model is investigated as a rotation may affect the properties of the antenna. The rotational effect is calculated as

$$20 \log_{10} \left( \sqrt{\Re(S_{11} - S_{11,rot})^2 + \Im(S_{11} - S_{11,rot})^2} \right) \quad (4.3.1)$$

where  $S_{11}$  is the reflection coefficient for the antenna placed aligned to the FDTD grid axis and  $S_{11,rot}$  is the reflection coefficient for the rotated antenna. The rotational effect for the transmission coefficient is calculated in the same way when the receiving antenna is placed on the opposite site of the reconstruction domain. In Figure 4.3.5 and Figure 4.3.6 the rotational effect is showing and the effect is below -80 dB for the transmission coefficient. However the antenna rotated  $45^\circ$  suffers from a noticeable effect in the reflection coefficient for frequencies above 1 GHz.

### 4.3. Modelling of the whole antenna array

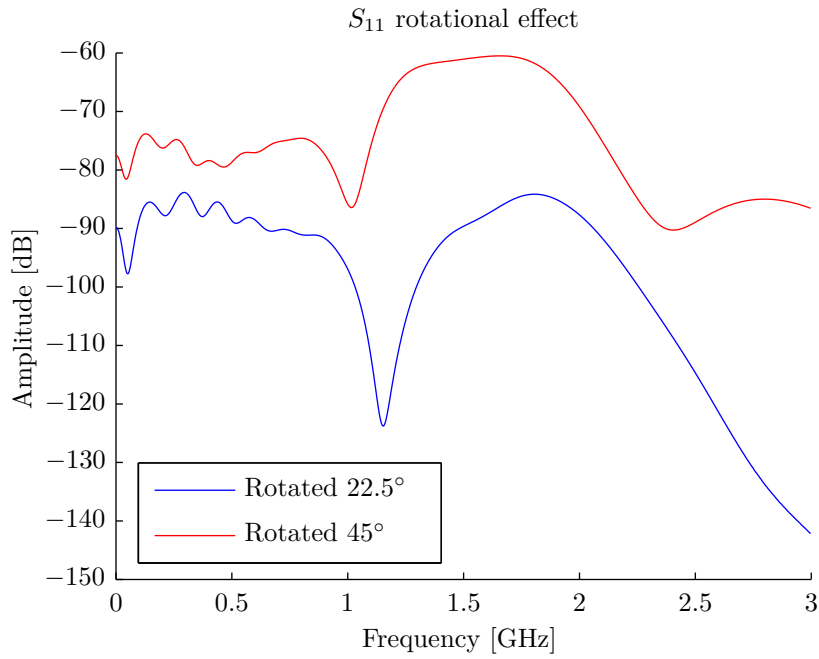


Figure 4.3.5: The rotational effect for the reflection coefficient,  $S_{11}$ .

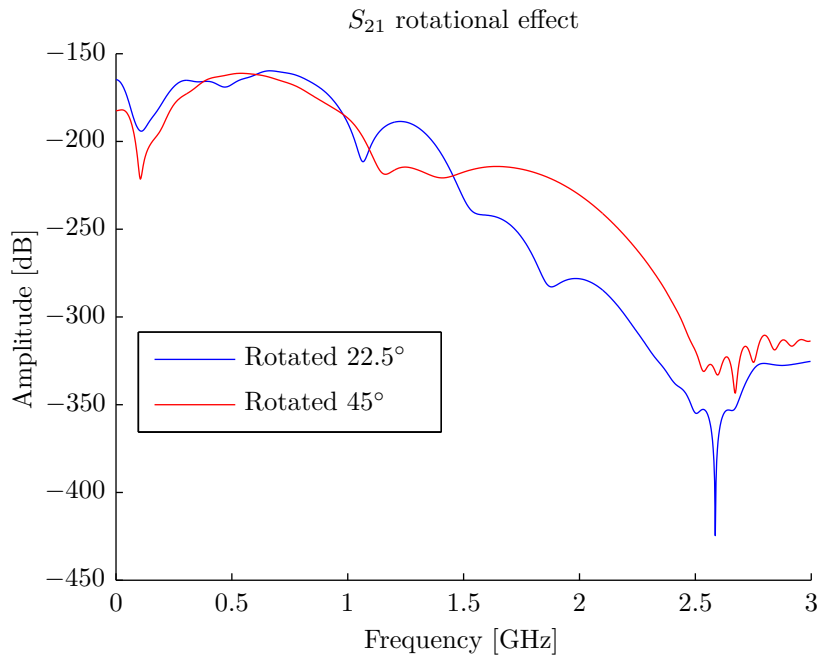


Figure 4.3.6: The rotational effect for the transmission coefficient,  $S_{21}$ .

### 4.3.2 Measurement compared to simulation

In this simulation the whole tank is used with all antennas placed as illustrated in Figure 4.3.3 and Figure 4.3.4. The liquid in the tank is water with added salt given a permittivity and conductivity as shown in Figure 4.3.7 and Figure 4.3.8. The antenna used in this simulation and measurement is the antenna with bent inner conductor with and without dielectric, see Figure 4.3.9. The reason for just including these two antennas is that the FDTD model was best in these two cases. The reflection and transmission curves for these two cases can be seen in Figure 4.3.10 and Figure 4.3.11. In water, there will be a high contrast between having the dielectric and not as the permittivity for the dielectric is  $\epsilon_{static} = 2.1$  and the water has a permittivity of  $\epsilon_{static} = 78.0$  and the contrast between the dielectric and the water is  $C = 2.1 : 78 = 1 : 37$ . In air the effect of the dielectric is not as noticeable as the contrast in permittivity between the dielectric and the air is  $C = 2.1 : 1$ .

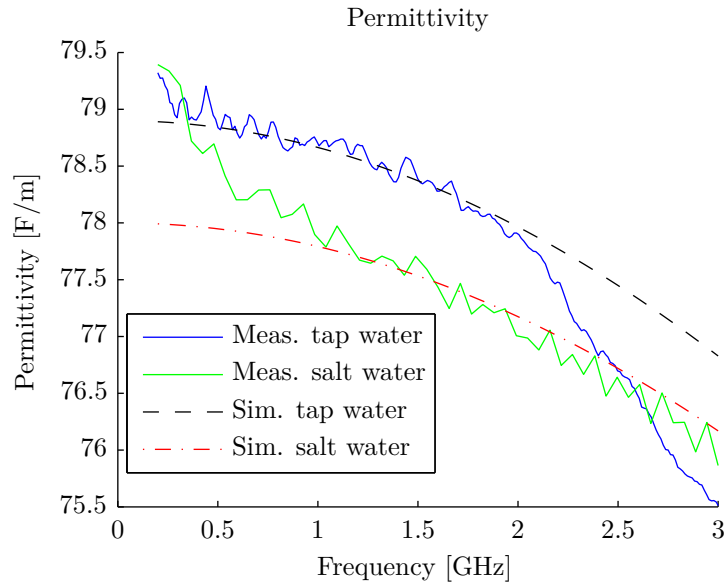


Figure 4.3.7: The measured and simulated permittivity for the liquid medium.

### 4.3. Modelling of the whole antenna array

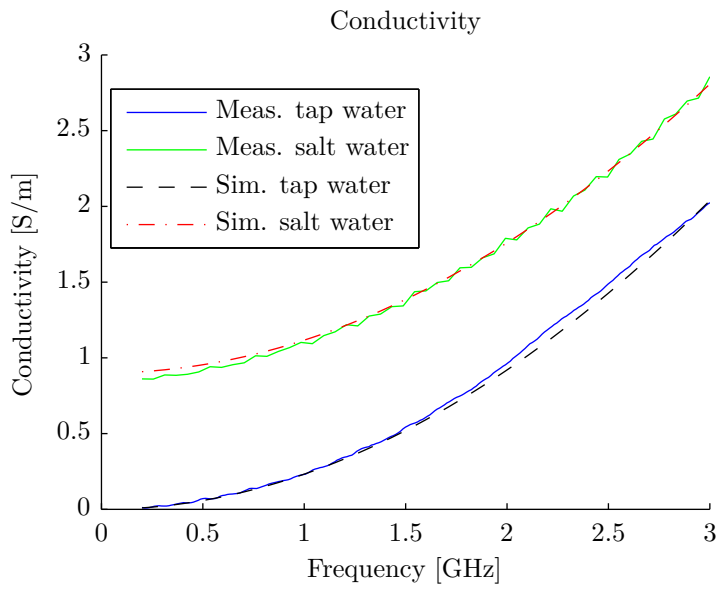


Figure 4.3.8: The measured and simulated conductivity for the liquid medium.

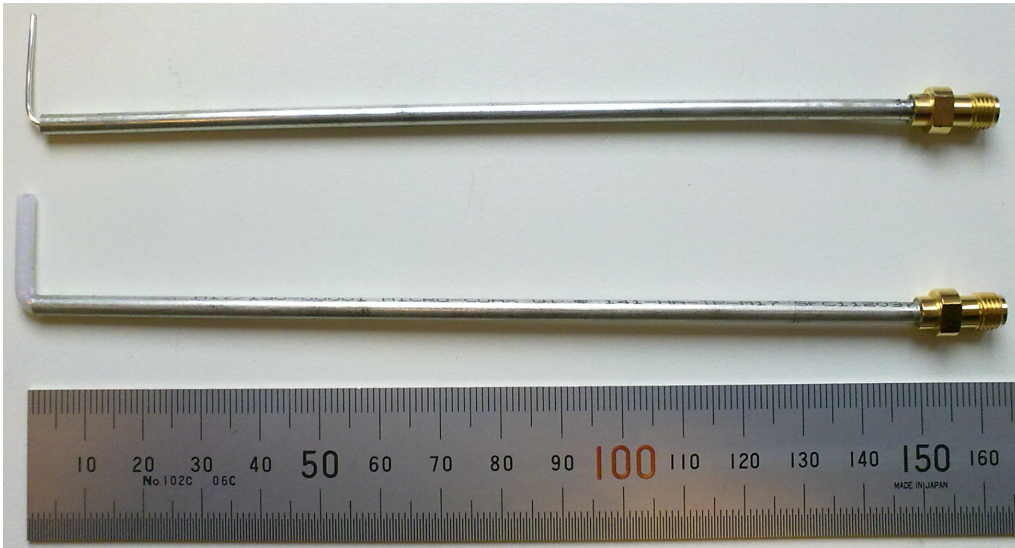


Figure 4.3.9: The antenna with cable and connector used during the measurements.

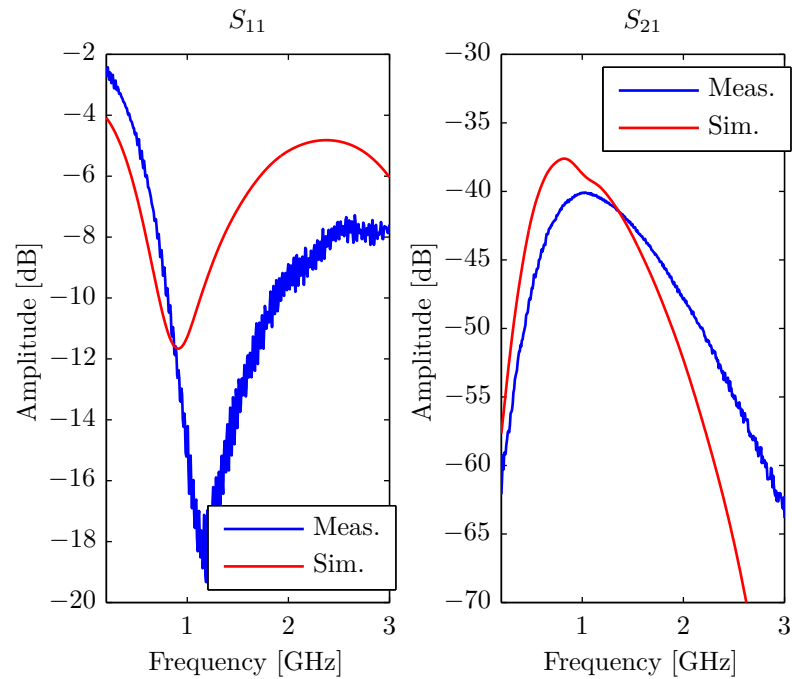


Figure 4.3.10: The measurement and simulation of the reflection- and transmission-coefficient for the first antenna with dielectric in the array.

In this simulation the antennas with dielectric was used and the grid cell size was set to 4 mm. The result was not successful in modelling of the reflection curve, the transmission curve was however much better. The reason for this is that the dielectric is harder to model and not even with a refinement of the FDTD grid cells by a 10th was enough. The antenna with the dielectric was not used even thou the properties of the antennas was better, the noise floor is higher up in frequency and the bandwidth is wider, as seen in Figure 4.3.10.

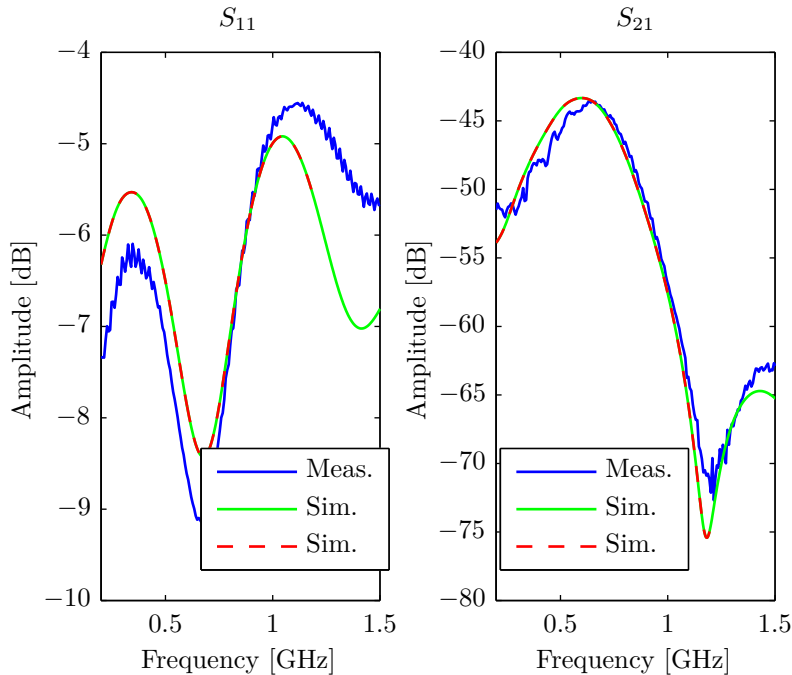


Figure 4.3.11: The measurement and simulation of the reflection- and transmission-coefficient for the first antenna without dielectric in the array.

The simulation without the dielectric on the inner conductor was done with a grid cell size of 4 mm and the result was more successful as both the reflection and the transmission curves are very similar to the measured ones. However at a frequency of 1.5 GHz the simulated reflection curve differs from the measured which gives a large model error. This can be avoided by using a lower frequency interval during the reconstruction. This is the dashed red curve shown in Figure 4.3.11.

## 4.4 Summary of antenna modelling

The chosen length on the inner conductor was 20 mm allowing for fine adjustment of the resonance frequency around 1.3 GHz for the antenna. The best model of the cables is the one shown in Figure 4.1.3 as the cable effect seen in Figure 4.1.6 is lowest both in the reflection-,  $S_{11}$ , and transmission-coefficient,  $S_{21}$ . This gives that the type of antenna is just the coaxial cable with the inner conductor bent upwards as active antenna.

The simulations shows that the edge effect can be neglected if the conductivity is increased for a tank with the antenna placed 110 mm from

#### 4. MODELLING OF THE ANTENNA ARRAY

---

the edge. This is due to the limited measurement capacity of the network analyser which has a noise floor of -80 dB. All signals below this level will be considered as noise and do not contribute to the measurements. The reason the edge effect is decreasing with increased conductivity is that the electric field gets damped due to currents induced in the water. However the whole tank must be modelled in the FDTD simulations as the cables are disturbing the signals.

The antennas is placed in four rings of eight antennas where every other ring is rotated by  $22.5^\circ$  and positioned 40 mm apart in z-direction. The tank size was determined to be 382 mm as inner diameter due to the fact that there was an acrylic cylinder of this size available. The antenna cables were then decided to be 120 mm which gives a measurement domain of 142 mm in diameter.

# Chapter 5

## Reconstructed images

The measurements are performed by placing an object in the tank with the antenna array. Only one of the antennas emits at a time and the others acts as receivers. This step is repeated until all antennas have emitted their signal and afterwards the reconstruction can be done. Before doing the reconstruction a measurement of an empty antenna system must be done, this is used as a reference to compensate for the slightly differences in the cables and connectors.

### 5.1 Homogeneous objects in water

The measurements with the tank filled with water were done with the antennas with bent inner conductor and with no dielectric surrounding the outer antenna tip, see Figure 4.1.3. Three measurements with different objects were done. In the first measurement an acrylic cylinder with radius of 7.5 mm was emerged vertical in the middle of the tank leaving a part of it above the water surface. The second measurement was performed with two acrylic cylinders with same dimensions as above. One of them was placed 19 mm from the first antenna and the other one was placed 19 mm from the fifth antenna leaving a distance of 50 mm in between. The third measurement was done with a plastic cup of average radius of 65 mm filled with pure ethanol submerge partially in the tank with 80 mm below the surface. In table 5.1 the different permittivity and conductivity for all objects is shown.

The reconstruction domain was then set to a radius of 44 mm leaving an offset to the antennas as the total measurement domain has a radius of 71 mm. The reason for having a smaller reconstruction domain is mainly that the antennas will interfere in the FDTD simulation if they are to

close and also that the reconstruction time is lowered. The reconstruction domain is limited in negative z-direction 64 mm below the lowest antenna ring as no information will be acquired as the scattering in this direction is low. In positive z-direction the water surface limits the reconstruction domain as there will be a high contrast in permittivity between the air and the water in the tank. During the first and the second reconstruction a Gaussian pulse with centre frequency 700 MHz and bandwidth of 500 MHz which corresponds the dashed red line in Figure 4.3.11. In the third reconstruction a pulse with centre frequency and bandwidth of 150 MHz was used.

	Acrylic cylinder	Ethanol
$\epsilon_\infty$	2.7	4.5
$\epsilon_{static}$	3.0	26.77
$\tau$	8.0e-12	1.4e-12

Table 5.1: The Debye properties of the acrylic cylinder and pure ethanol.

### 5.1.1 One small object

The reconstruction of a small acrylic cylinder is shown below. In Figure 5.1.1 the full reconstruction domain is illustrated with two slices crossing in the objects centre. This representation of data gives an overview of the object and in Figure 5.1.2 and Figure 5.1.3 a 2D representation of several xy-planes shows the object form. These xy-planes are shown for six different z-heights where the first placed 32 mm under the first antenna ring and the last just under the water surface. The reconstructed measurement data shows good similarity to the reconstruction of simulated data for the permittivity, however there are a lot of artefacts in the reconstruction of measured data for the conductivity. This is shown even for simulated data which suffer from a ringing artefact with higher conductivity surrounding the object. The imaging in the vertical direction is good both for the conductivity and the permittivity, however when imaging directly below the water surface the imaged object is larger and the contrast lower. The permittivity of the measured object is consider successfully imaged even if the contrast between the object and the background is lower that for the modelled permittivity. The low contrast is a limitation that is caused by the reconstruction algorithm when using a high conductivity liquid medium.

## 5.1. Homogeneous objects in water

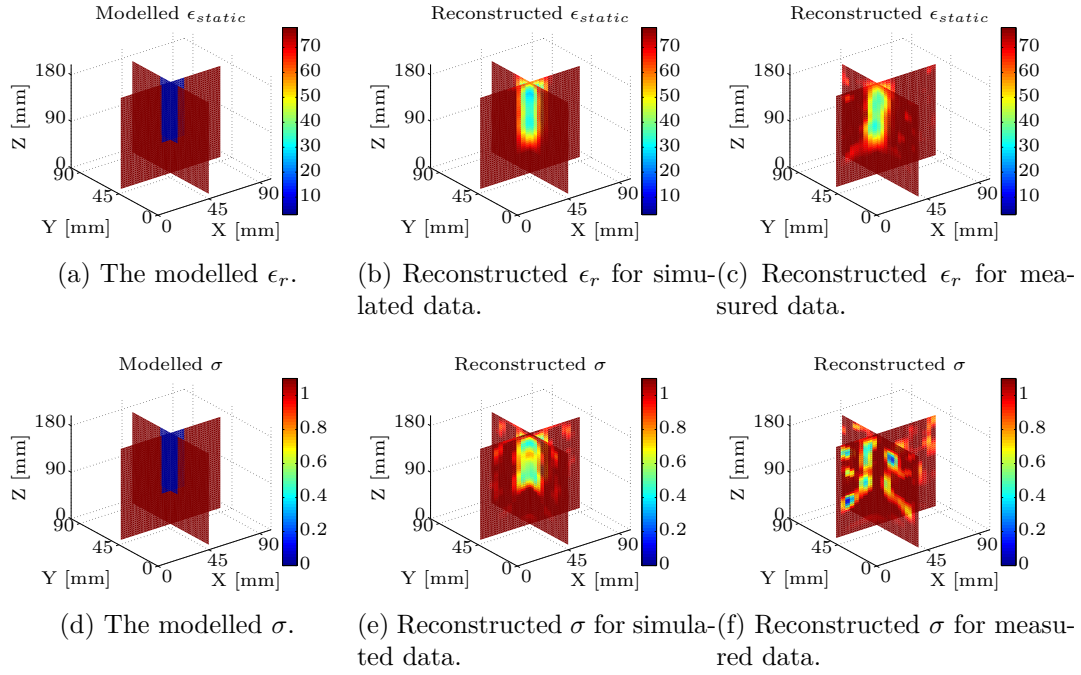


Figure 5.1.1: The 3D representation of the model used and the reconstructions of measured and simulated data.

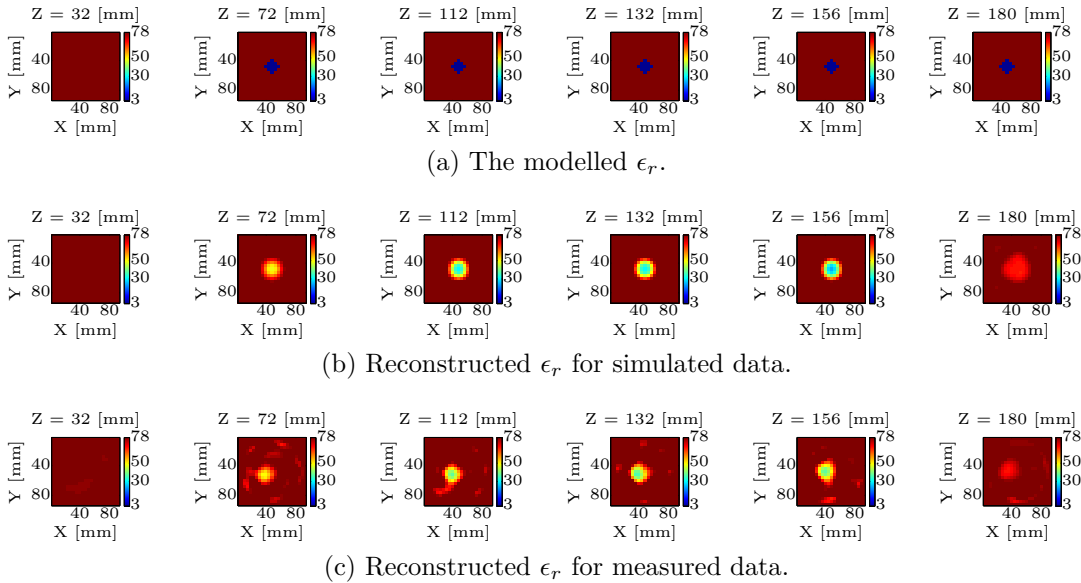


Figure 5.1.2: The 2D representation in different z-heights of the reconstructions of measured and simulated data.

## 5. RECONSTRUCTED IMAGES

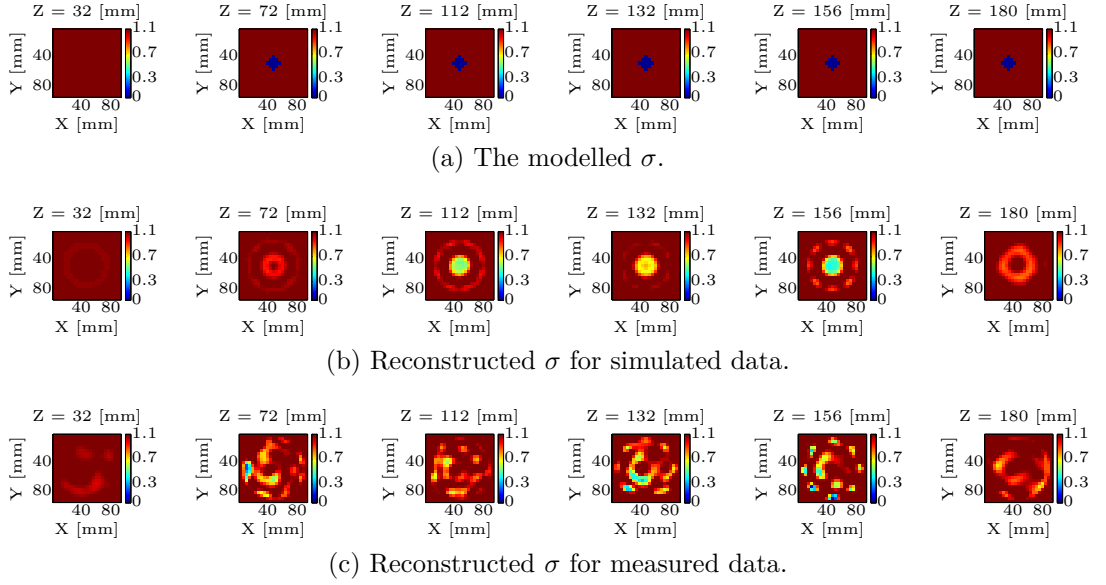


Figure 5.1.3: The 2D representation in different z-heights of the reconstructions of measured and simulated data.

### 5.1.2 Two small objects

The reconstruction of two small acrylic cylinders is shown below, for the reconstruction of simulated data a 12 mm larger reconstruction domain radius is used when reconstructing the conductivity. This is because the reconstruction algorithm is not able to do a single iteration before it fails and in this case it fails on the 8th iteration. In both the reconstruction of simulated and measured data there are artefacts. For the permittivity it is however possible to see the two objects both for the simulated data and the measured. The reconstructed conductivity suffers from artefacts and the object is not well reconstructed. There are also several small circular artefacts that are caused by the antennas in the FDTD model, this is clearly seen in Figure 5.1.6b and Figure 5.1.6c. The reconstructed permittivity for the measured data is better in this case as the contrast is higher. The reason for this is because the objects are closer to the antennas and the signal reflected from the object is higher.

## 5.1. Homogeneous objects in water

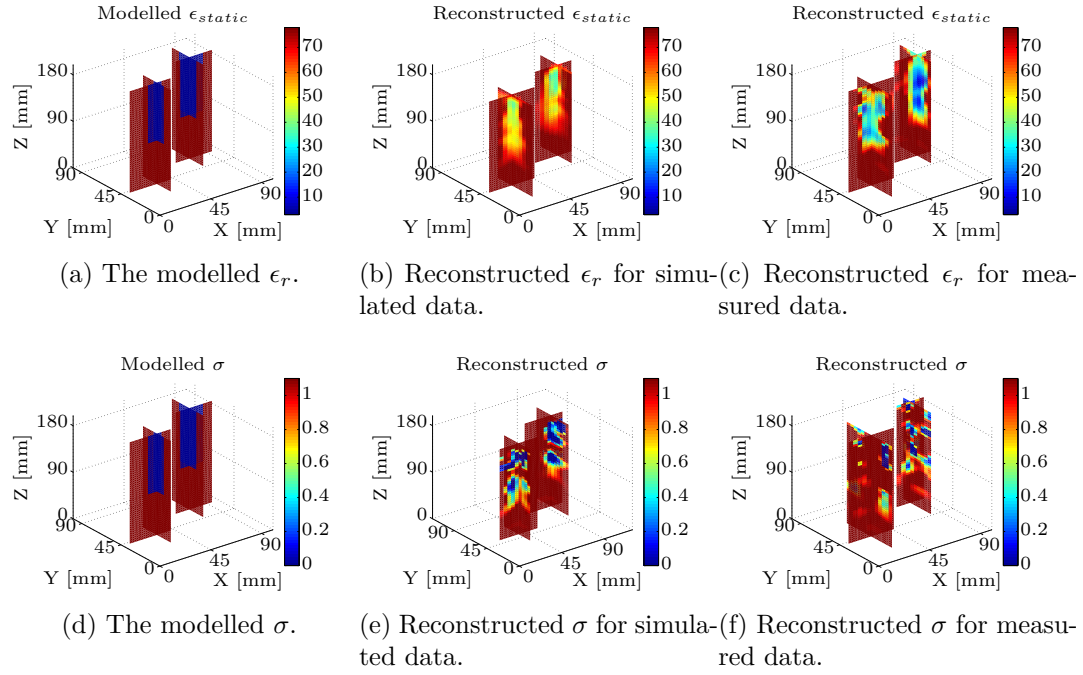


Figure 5.1.4: The 3D representation of the model used and the reconstructions of measured and simulated data.

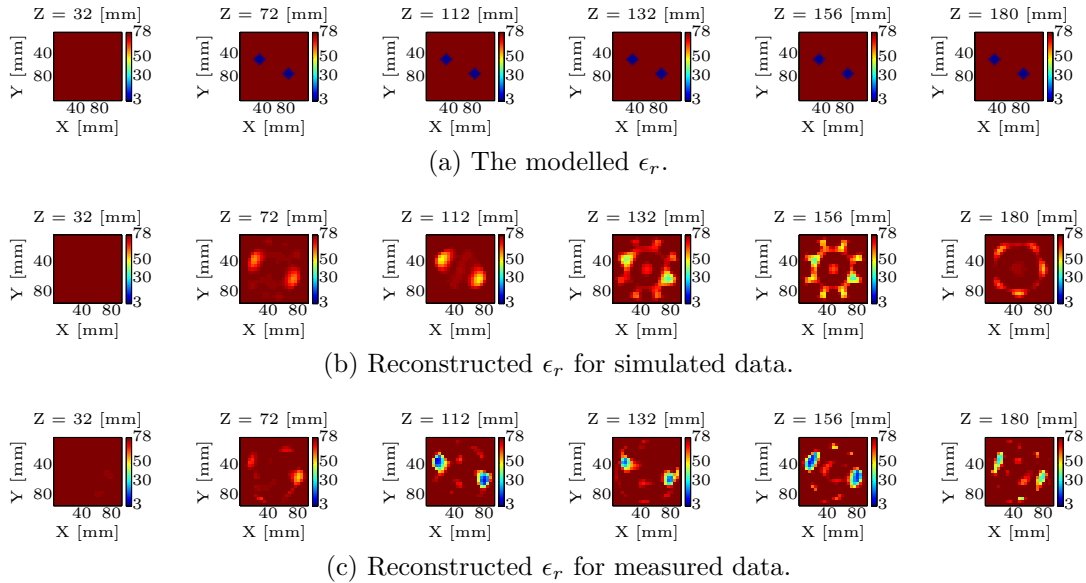


Figure 5.1.5: The 2D representation in different z-heights of the reconstructions of measured and simulated data.

## 5. RECONSTRUCTED IMAGES

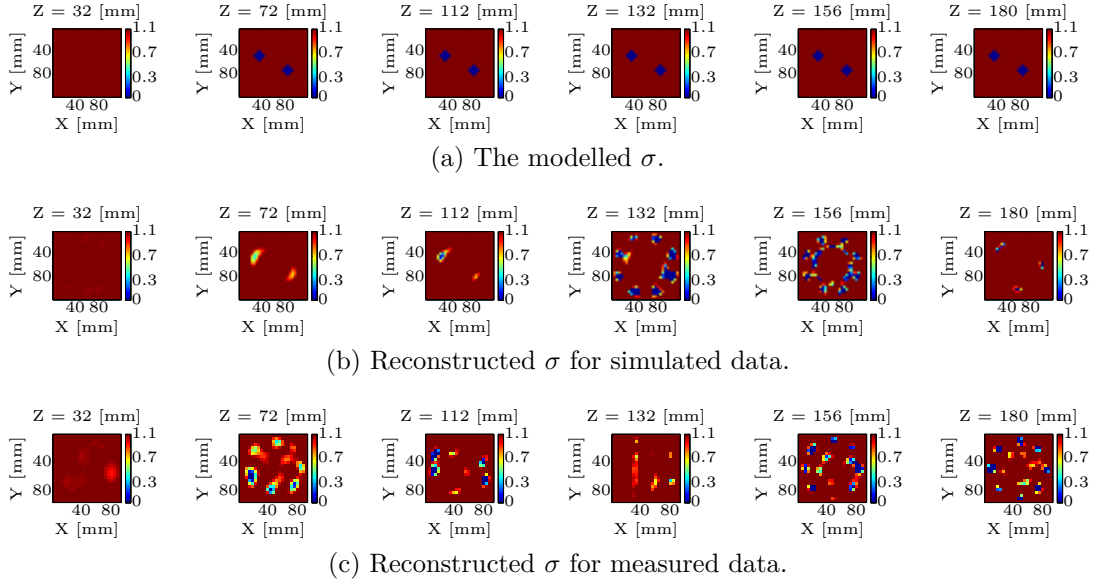


Figure 5.1.6: The 2D representation in different z-heights of the reconstructions of measured and simulated data.

### 5.1.3 One large object

The reconstruction of one large object has a 12 mm larger reconstruction domain radius when reconstructing the conductivity for measured data and again the algorithm is not able to achieve 10 iterations so instead the 9th is shown. For the larger object a lower frequency is used to increase the accuracy for the reconstructions. This is because the object is bigger and the wavelength that best detects the object is then higher. If the same pulse as above is used the reconstructions will suffer from an artefact making a hole in the object, this is shown in Figure 5.1.10 and Figure 5.1.11 so instead a pulse with centre frequency and bandwidth of 150 MHz is used. In this case the image of the simulated data shows a better result than for the measured. The conductivity for the measured data is not well reconstructed and for the permittivity the contrast is not constant in the object. For the reconstruction of simulated data the image of the conductivity is slightly larger and hollow but for the permittivity the object is successfully reconstructed, however the contrast is lower in vertical endpoints of the object.

## 5.1. Homogeneous objects in water

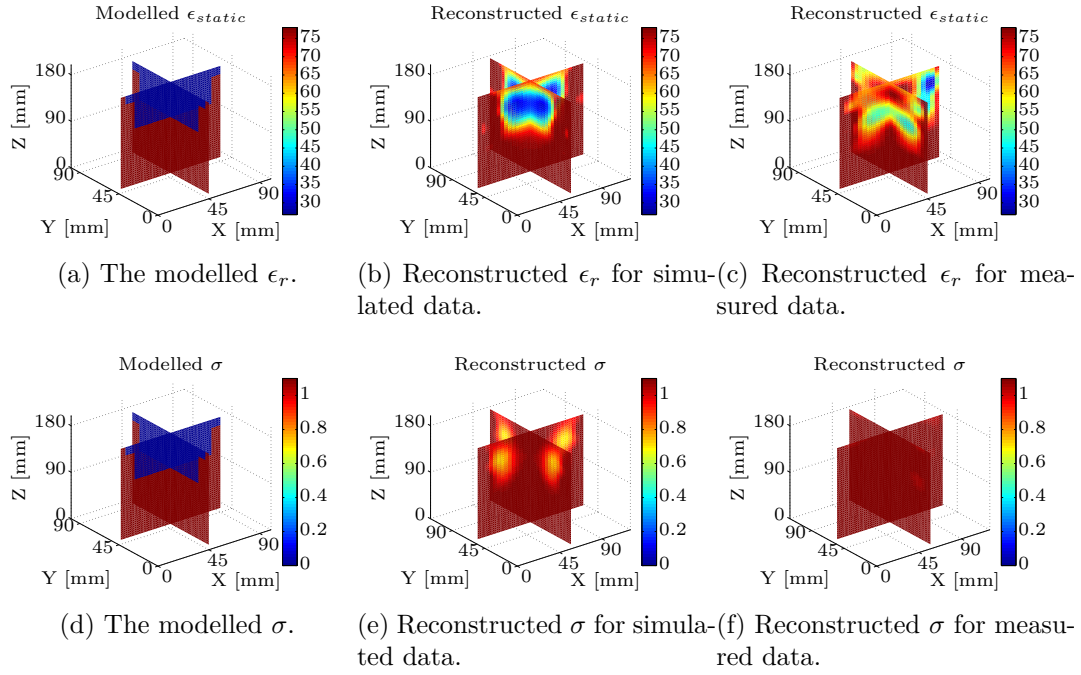


Figure 5.1.7: The 3D representation of the model used and the reconstructions of measured and simulated data.

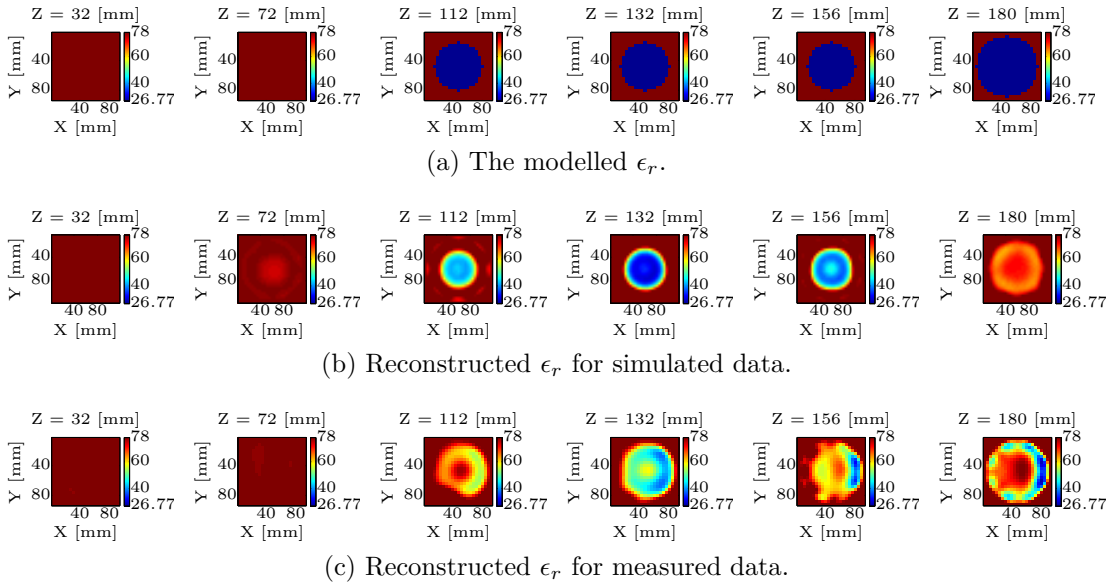


Figure 5.1.8: The 2D representation in different z-heights of the reconstructions of measured and simulated data.

## 5. RECONSTRUCTED IMAGES

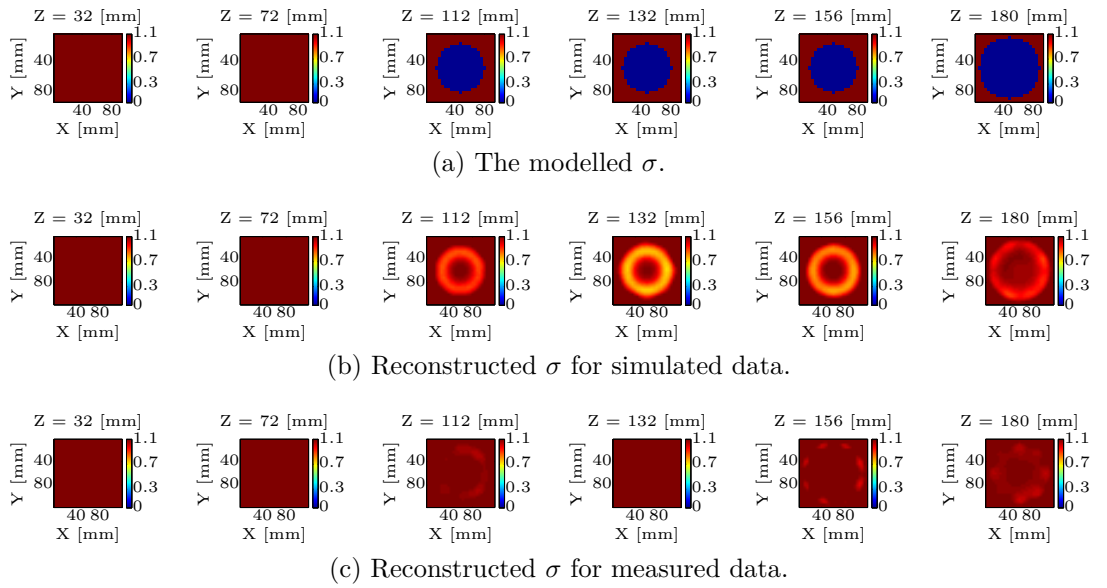


Figure 5.1.9: The 2D representation in different z-heights of the reconstructions of measured and simulated data.

When the pulse with centre frequency 700 MHz and bandwidth 500 MHz was used the reconstructed object became hollow. The contrast of the object is however better reconstructed for the measured data for both the permittivity and the conductivity as well as the conductivity for the simulated data.

## 5.1. Homogeneous objects in water

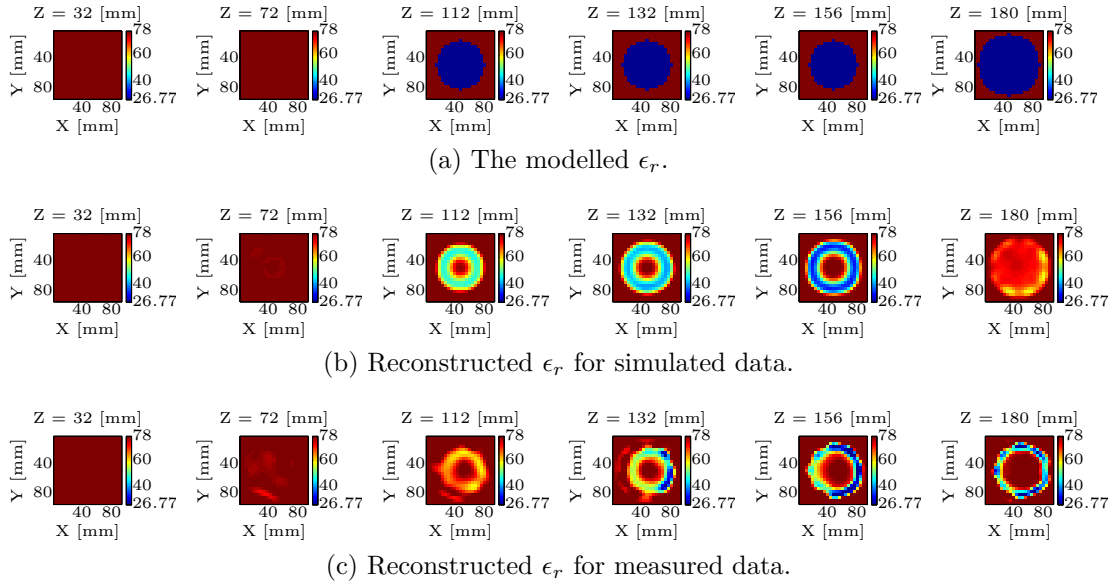


Figure 5.1.10: The 2D representation in different z-heights of the reconstructions of measured and simulated data.

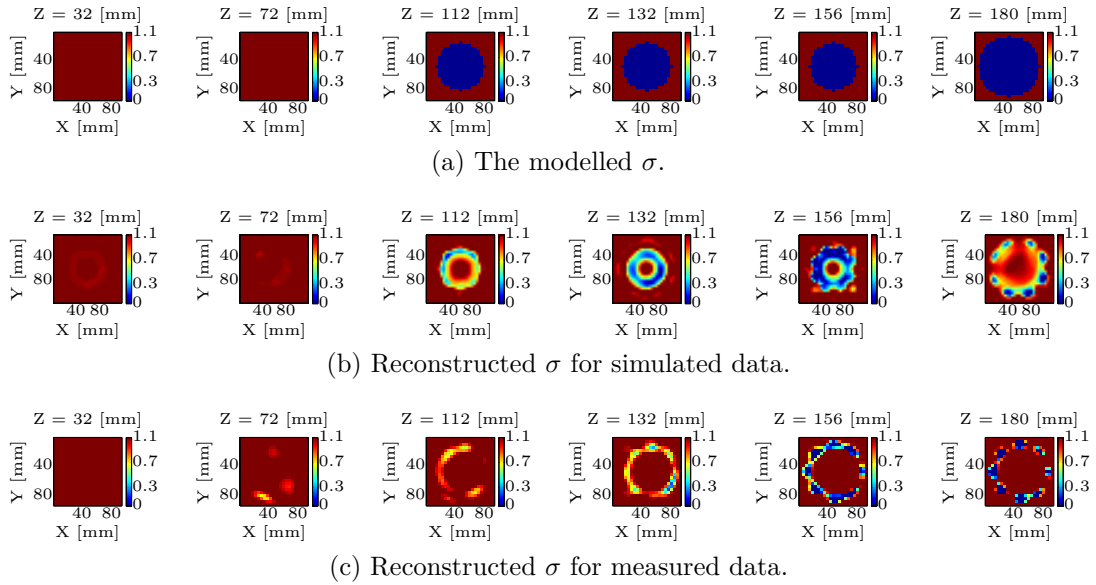


Figure 5.1.11: The 2D representation in different z-heights of the reconstructions of measured and simulated data.

### 5.1.4 Evaluation of measurements

The result was evaluated in two different ways, the first way was to only plot the functional value versus the amount of iterations made. In this way it is easy to see if the algorithm has converged, the result will not be better with more iterations. During the reconstruction of the conductivity for the simulated data of the two acrylic cylinders the reconstruction algorithm failed on the 9th iteration and during the reconstruction of the conductivity for the measured data of the cup of ethanol the algorithm failed at the 8th iteration. This is why there are gaps in the graphs below. The most important to see in Figure 5.1.12 is when there is a drop in the functional value, this is however not a good method of comparing different reconstructed objects as there is no information of how good the result is. Instead another way of evaluation is to formulate a relative error for the permittivity

$$\delta(\epsilon_{static}) = \frac{\iiint_V |\epsilon_{rec}(\mathbf{x}) - \epsilon_{true}(\mathbf{x})| dV}{\iiint_V |\epsilon_{true}(\mathbf{x}) - \epsilon_{back}| dV} \quad (5.1.1)$$

and for the conductivity

$$\delta(\sigma) = \frac{\iiint_V |\sigma_{rec}(\mathbf{x}) - \sigma_{true}(\mathbf{x})| dV}{\iiint_V |\sigma_{true}(\mathbf{x}) - \sigma_{back}| dV} \quad (5.1.2)$$

where  $V$  is the volume of the reconstruction domain,  $\epsilon_{back}$  is the permittivity for the background and  $\sigma_{back}$  is the conductivity for the background. This evaluation is better to compare how well the reconstruction represents the measured object. These relative errors are plotted in Figure 5.1.13 were the relative error for the cup of ethanol is low and the relative error for the two cylinders are lower than for the case with only one cylinder. This compare well with the image obtained as the reconstructed values are better even though the shape is better for the case with only one cylinder. This is mainly due to that the objects are closer to the antennas in the case with two cylinders. Determined both by visual inspection of the image and the magnitude of relative error the reconstructed image of the conductivity is consistently not successful for any object.

## 5.1. Homogeneous objects in water

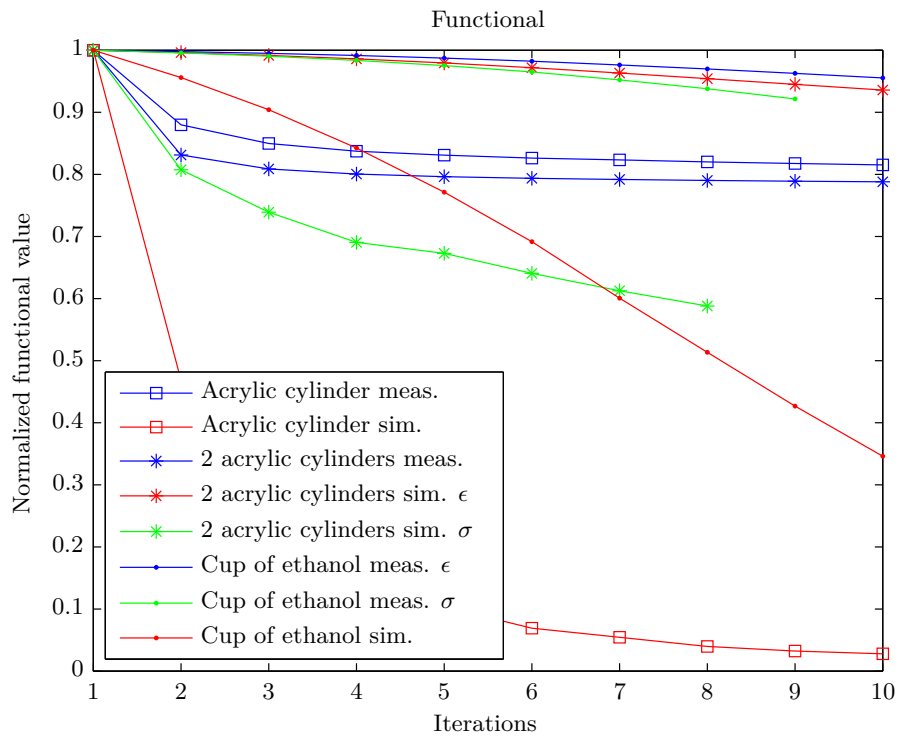


Figure 5.1.12: The functional for the three measurements.

## 5. RECONSTRUCTED IMAGES

---

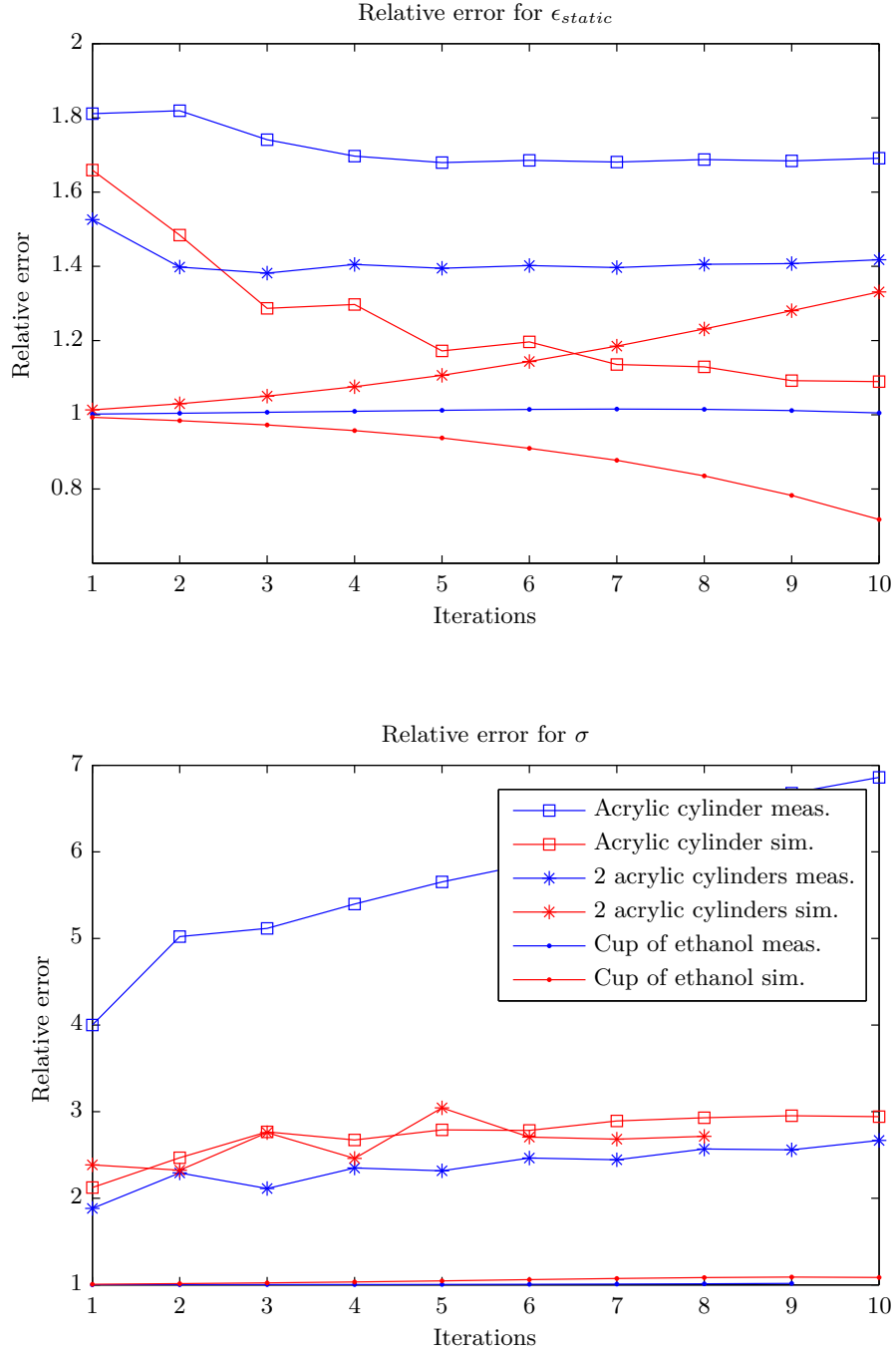


Figure 5.1.13: The relative error for the three measurements.

# Chapter 6

## Conclusion

In this thesis two different antennas were used during the measurements, one with dielectric on the inner conductor and one without. The reflection coefficient for the antenna with the dielectric was not successfully modelled and this is mainly due to that the FDTD grid cell cannot be small enough to model the dielectric. The dielectric has a thickness of 1.35 mm and a refinement of the grid cells to 0.4 mm did not solve the problem. Another refinement of the grid cell is not possible as the memory and time consumption will be far too high. These limitations of the FDTD grid size could be changed by refinement of the grid cells close to the antennas as the reflection is more effected of the medium and the change in medium close to the antenna. The antenna with dielectric showed better properties as the bandwidth is wider and the reflection is lower at the resonance frequency so further development of the FDTD simulator could increase the overall performance.

The antenna without dielectric used in this thesis shows good results when using a FDTD grid cell of 4 mm. Both the reflection coefficients and the transmission coefficients are satisfyingly modelled when a Gaussian pulse with centre frequency of 700 MHz and bandwidth of 500 MHz are used as a source in the transmitting antenna. This model was used in the reconstruction of a homogeneous acrylic cylinder of radius 7.5 mm when salt water was used as a liquid medium in the tank and gives a satisfying image of the permittivity, however the image of the conductivity is not accurate.

The same model was also used to reconstruct a measurement of two acrylic cylinders with a radius of 7.5 mm with also promising result for the permittivity but not for the conductivity. The third measurement was performed on a cup of ethanol which gave a good result for the permittivity when a pulse with centre frequency 150 MHz and bandwidth 150 MHz was used, however the conductivity was not well reconstructed.

## 6. CONCLUSION

---

The prototype was intentionally made for clinical microwave tomography and proper clinical testing still resides in the future. The reconstructions of the permittivity are well made for both small and large cylindrical objects and can therefore be expected to detect tumours in a breast. A suggested test is to develop a phantom of a breast with a tumour with similar dielectric properties as a real one. Finally, the conclusion that the described imaging system array can be used for clinical use in competition to traditional X-ray imaging cannot be made.

# References

- [1] P. Boyle and B. Levin, “World cancer report 2008,” pp. 412–416, 2008.
- [2] P. M. Meaney, M. W. Fanning, T. Raynolds, C. J. Fox, Q. Fang, C. A. Kogel, S. P. Poplack, and K. D. Paulsen, “Initial clinical experience with microwave breast imaging in women with normal mammography,” *Academic Radiology*, vol. 14, no. 2, pp. 207–218, 2007.
- [3] A. Fhager, S. K. Padhi, and J. Howard, “3D image reconstruction in microwave tomography using an efficient FDTD model,” *Antennas and Wireless Propagation Letters, IEEE*, vol. 8, pp. 1353–1356, 2009.
- [4] P. Meaney, M. Fanning, T. Zhou, A. Golnabi, S. Geimer, and K. Paulsen, “Clinical microwave breast imaging - 2D results and the evolution to 3D,” pp. 881–884, 2009.
- [5] H. Fricke and S. Morse, “The electric capacity of tumors of the breast,” *J Cancer Res*, vol. 16, pp. 340–376, 1926.
- [6] A. C. Kak and M. Slaney, *Principles of Computerized Tomographic Imaging*. IEEE Press., 1988.
- [7] K. S. Yee, “Numerical solution of initial boundary value problems involving Maxwell’s equations in isotropic media,” *Antennas and Propagation, IEEE Transactions on*, vol. 14, pp. 302–307, may. 1966.
- [8] A. Taflove and M. E. Brodwin, “Numerical solution of steady-state electromagnetic scattering problems using the time-dependent Maxwell’s equations,” *Microwave Theory and Techniques, IEEE Transactions on*, vol. 23, pp. 623–630, aug. 1975.
- [9] A. Taflove and S. C. Hagness, *Computational Electrodynamics: The Finite-Difference Time-Domain Method*. Artech House Inc, third ed., 2005.

## REFERENCES

---

- [10] A. Fhager, *Microwave Tomography*. PhD thesis, Chalmers University of Technology, 2006.
- [11] A. Taflove, K. R. Umashankar, B. Beker, F. Harfoush, and K. S. Yee, "Detailed FD-TD analysis of electromagnetic fields penetrating narrow slots and lapped joints in thick conducting screens," *Antennas and Propagation, IEEE Transactions on*, vol. 36, pp. 247–257, feb. 1988.
- [12] R. Holland and J. W. Williams, "Total-field versus scattered-field finite-difference codes: A comparative assessment," *IEEE Transactions on Nuclear Science*, vol. 30, no. 6, pp. 4583–4588, 1983.
- [13] J.-P. Berenger, "A perfectly matched layer for the absorption of electromagnetic waves," *Journal of Computational Physics*, vol. 114, no. 2, pp. 185–200, 1994.
- [14] D. S. Katz, E. T. Thiele, and A. Taflove, "Validation and extension to three dimensions of the Berenger PML absorbing boundary condition for FD-TD meshes," *IEEE Microwave and Guided Wave Letters*, vol. 4, no. 8, pp. 268–270, 1994.
- [15] J. A. Roden and S. D. Gedney, "Convolution PML (CPML): An efficient FDTD implementation of the CFS-PML for arbitrary media," *Microwave and Optical Technology Letters*, vol. 27, no. 5, pp. 334–339, 2000.
- [16] J.-P. Berenger, *Perfectly matched layer (PML) for computational electromagnetics*. Morgan & Claypool, first ed., 2007.
- [17] G. Camelia, *Bioengineering and Biophysical Aspects of Electromagnetic Fields*, ch. 3 Dielectric Properties of Biological Materials. CRC Press, third ed., 2006.
- [18] K. S. Cole and R. H. Cole, "Dispersion and absorption in dielectrics i. alternating current characteristics," *The Journal of Chemical Physics*, vol. 9, no. 4, pp. 341–351, 1941.
- [19] K. S. Cole and R. H. Cole, "Dispersion and absorption in dielectrics: Ii. direct current characteristics," *The Journal of Chemical Physics*, vol. 10, no. 2, pp. 98–105, 1942.
- [20] M. Hiebel, *Fundamentals of Vector Network Analysis*. Rohde & Schwarz GmbH & Co. KG, second ed., 2007.

- [21] A. Fhager, A. Romputtal, and M. Persson, “Antenna system for clinical microwave tomography,” 2010.
- [22] Y. Huangl and B. Kevin, *Antennas: From Theory to Practice*. John Wiley & Sons Ltd, 2008.
- [23] D. K. Cheng, *Field and wave electromagnetics*. Addison-Wesley Publishing Company, Inc., second ed., 1989.